Kinetic modeling of CO assisted passive NO<inf>x</inf> adsorption on Pd/SSZ-13

Chemical Engineering Journal 428 (2022) 132459

Contents lists available at ScienceDirect

Chemical Engineering Journal

journal homepage: www.elsevier.com/locate/cej

Kinetic modeling of CO assisted passive NO_x adsorption on Pd/SSZ-13

Dawei Yao [a], Rojin Feizie Ilmasani [a], Johann C. Wurzenberger [b], Thomas Glatz [b], Joonsoo Han [a], Aiyong Wang [a], Derek Creaser [a], Louise Olsson [a,*]

[a] Chemical Engineering Division, Competence Center for Catalysis, Chalmers University of Technology, Göteborg, SE, 41296, Sweden
[b] AVL List GmbH, Graz, Austria

ARTICLE INFO

Keywords:
Passive NO_x adsorber (PNA)
CO effect
Pd/SSZ-13
Kinetic modelling

ABSTRACT

Passive NO_x adsorption (PNA) has been recently developed as a promising technology for controlling the NO_x emissions during the cold start period. In this work, we illustrate a CO-assisted mechanism by combining experimental and kinetic modeling studies. Pd/SSZ-13 has been synthesized, characterized and evaluated as a PNA in low-temperature NO_x adsorption and temperature program desorption cycles, to represent multiple cold start periods. The gas compositions were also systemically changed, where both the effect of varying NO_x and CO feed was evaluated in the presence of high water and oxygen contents. A kinetic model was developed to simulate the profiles of NO and NO_2, including three initial Pd sites ($Z^-Pd(II)Z^-$, $Z^-[Pd(II)OH]^+$ and PdO). It is concluded from XPS and in situ DRIFTS experiments, flow reactor measurements and modelling observations that CO reduces Pd(II) species to Pd(I)/Pd(0) species, which increases the stability of the stored NOx species, resulting in a release above the urea dosing temperature. The model could well describe the experimental features, including the effect of CO. In addition, the model was used for full-scale catalytic converter simulations.

1. Introduction

The market of vehicles has largely increased with the growth of the global economy, accompanied with rising concerns for the produced NO_x [1]. NO_x emissions from vehicles can be reduced significantly using techniques, such as NH_3 Selective catalytic reduction (SCR) [2,3] and Lean NO_x traps (LNT) [4,5]. However, with kinetic restrictions at low temperature for lean NO_x traps and the issue of ineffective urea dosing at low temperature (<200 °C) for SCR, neither of the systems can effectively control NO_x emissions during the cold start period [6]. Therefore, a promising technology was recently developed to employ a Passive NO_x absorber (PNA) upstream of the SCR unit in the aftertreatment system. The NO_x in the exhaust is stored in the PNA at low temperature during the cold start period. Thereafter, it is thermally released at higher temperature (at and above ~ 200 °C), which is feasible for urea dosing [7,8] at which the NO_x is subsequently converted in the SCR process.

There is a growing interest in Pd zeolites for PNA due to their tolerance to H_2O and sulfur [6,9]. Particularly, small-pore zeolites with palladium, such as SSZ-13, have been shown to be an effective material with a relatively high NO_x desorption temperature [10,11]. The basic understanding of NO_x adsorption on Pd based zeolites under conditions including $NO_x + O_2 + H_2O$, with or without CO, has been initially developed. It was found that the adsorption sites were mainly ionic Pd^{2+} in the zeolite framework ($Z^-Pd(II)Z^-$ and $Z^-[Pd(II)OH]^+$) and PdO_x sites on the external surfaces of the zeolites [12–15]. Oxygen is present in almost all reported passive NO_x adsorption tests since a high level of oxygen is always present in diesel and lean-burn gasoline vehicle exhausts. The O_2 accelerates nitrate formation and NO_x adsorption [13], also it triggers the regeneration of the PNA under higher temperature [16]. The presence of H_2O has also been reported to severely suppress the NO_x adsorption on Pd sites at 80 ~ 100 °C, and inhibit the adsorption of multiple NO_x species on single Pd sites [12,17]. Although it is widely reported that an increased adsorption of NO_x and higher desorption temperature appears after adding CO [12,13,18,19], no consensus has been reached on the precise roles of CO on passive NO_x adsorption. Some of the recent works demonstrated that the presence of CO resulted in more stable NO species due to either simultaneous NO and CO co-adsorption, or that CO reduces the Pd phase [8,12,20,21]. It should also be mentioned that under high CO concentrations it has been recently found that Pd/zeolites deactivate [22].

To further investigate the reaction mechanism of PNA a few kinetic models have been developed. Ambast et al [16]. developed a kinetic model for a PNA process using H/ZSM-5 and Pd/ZSM-5, focusing on the change of Pd species during PNA tests under gas mixtures including 5

* Corresponding Author.
E-mail address: louise.olsson@chalmers.se (L. Olsson).

https://doi.org/10.1016/j.cej.2021.132459
Received 28 May 2021; Received in revised form 31 August 2021; Accepted 9 September 2021
Available online 17 September 2021

ppm NO_2 / 400 ppm NO / 2% O_2/ 7% H_2O. Furthermore, they further developed a kinetic model in their recent paper [23] using Pd/SSZ-13 including 2 initial Pd sites (Z-Pd^{2+}Z-, $Z^-[PdOH]^+$), as the active sites during uptake of NO, CO and C_2H_4. A PNA kinetic model using PtPd/CeO_2-ZrO_2 was also developed, proving that the NOx could be adsorbed on Ce^{x+} forming nitrites and nitrates [24].

Herein, based on the aforementioned experimental and kinetic modeling study, we are establishing a kinetic model which can describe the NO_x storage behavior in multicycle PNA test under different NO_x and CO concentrations. Experimentally we find an irregular effect by changing CO concentration, influencing the reaction network, which also needs to be described our developed model. In addition, another objective in this work is to ascertain the precise role of CO addition in enhancing NO_x stability based on experiments and kinetic modelling. Pd/SSZ-13 was synthesized and tested for multi-cycle NO_x adsorption and temperature program desorption (TPD) experiments with varying inlet gas composition (200–400 ppm NO_x, 0–400 ppm CO, 8%O_2, 5% H_2O). Characterizations were conducted for the as-prepared catalyst and the spent catalyst to gain insight into the Pd species during the multi-cycle PNA test. Three initial Pd sites, $Z^-Pd(II)Z^-$, $Z^-[Pd(II)OH]^+$ and PdO were used as a base for the model. It was concluded from both experiments and kinetic modelling that low concentrations of CO reduced Pd(II) sites to lower valence Pd(I)/Pd(0), subsequently enhancing the adsorption of NO_x. The model could describe the experimental findings well. Furthermore, a full-scale catalytic converter model was further developed to demonstrate the influence of spatial and temporal temperature gradients on PNA during cold-start simulations.

2. Experimental methods

2.1. Catalysts synthesis

SSZ-13 with Si/Al = 12 was synthesized according to a previously reported hydrothermal method [25,26]. Briefly, 0.8 g NaOH (Sigma-Aldrich) was first dissolved into 66 g deionized water, then 17.68 g of the structure directing agent (TMAda-OH, Sigma-Aldrich) was added into the mixture while stirring. Subsequently, 1.38 g $Al(OH)_3$ (Sigma-Aldrich) and 12 g fumed silica (7 nm average particle size, Sigma-Aldrich) were added into the mixture with vigorous stirring until the gel was fully homogenized. The gel was then sealed into two 75 mL autoclaves (stainless steel using a Teflon liner). Then the autoclaves were put into sand baths on hot plates with continuous stirring, and kept at 160 °C for 96 h. After the hydrothermal synthesis the sample was separated and washed 3 times with deionized water, separated using centrifugation, and then dried at 120 °C overnight. The produced powder was then calcinated in static air at 600 °C for 8 h to obtain Na-SSZ-13. H-SSZ-13 was obtained by ion-exchange of the Na-SSZ-13. Briefly, the Na-SSZ-13 powder was mixed with 100 mL deionized water and 43.2 g NH_4NO_3 and heated to 80 °C in a water bath for 2 h. Then the sample was separated and washed via centrifugation. This ion-exchange procedure was repeated twice to ensure the Na^+ cations were fully exchanged by NH_4^+. Then the sample was dried at 120 °C overnight and calcined at 600 °C for 8 h to obtain H-SSZ-13.

Pd was added to the SSZ-13 by the incipient wetness impregnation method using $Pd(NO_3)_2$ solution to obtain 1 wt% Pd loading. After the impregnation, the sample was dried at 100 °C overnight and subsequently calcinated at 500 °C for 5 h in air.

2.2. Monolith preparation

The synthesized Pd/SSZ-13 was coated on a honeycomb-structured cordierite monolith with a cell density of 400 cpsi. The cordierite monolith was first cut to a uniform cylinder with a length of 2 cm and a diameter of 2.1 cm, followed by calcination at 550 °C for 2 h to remove any contaminants. The Pd/SSZ-13 powder was mixed with boehmite binder (Dispersal P2) with a ratio of 95:5 (weight), then dissolved into 1:1 ethanol/water (volume ratio) to obtain a slurry. The slurry was deposited by droplets spread over all the channels of monoliths until the slurry began to completely pass through all the channels. After deposition, the excess slurry was purged out using a flow of hot air at 90 °C. The coating and purging process was repeated until the loading of the washcoat reached 700 mg. Subsequently the coated monoliths were calcined at 500 °C for 5 h.

2.3. Characterization

The Pd, Si and Al content of the catalysts was analyzed using Inductively coupled plasma sector field mass spectrometry (ICP-SFMS). These measurements were conducted by ALS Scandinavia AB.

The pore structure of the samples was determined at 77 K by a N_2 adsorption–desorption method using a Micromeritics Tristar II 3000 Analyzer. The Brunauer-Emmett-Teller (BET) method was applied to determine the specific surface area.

Environmental scanning electron microscopy and corresponding energy-dispersive X-ray spectroscopy (ESEM-EDS) analyses of the coated monoliths were obtained with a Quanta200 ESEM equipped with an Energy dispersive Xray (EDX) system (Oxford Inca).

X-ray diffraction (XRD) analysis was conducted with a SIEMENS diffractometer D5000 operating at 40 kV and 40 mA, employing the graphite-filtered Cu Kα radiation (λ = 1.5418 Å) at room temperature. The samples were scanned from 5° to 50° with a rate of 1°/min.

X-ray photoelectron spectroscopy (XPS) analysis was conducted using a PHI5000 VersaProbe III-Scanning XPS Mircroprobe™ with an X-ray source of monochromatic AlKα X-ray (hν = 1486.6 eV). Energy resolution with 100 μm beam (i.e. FWHM) was 0.673 eV. The system was aligned with Au (83.96 eV), Ag (368.21 eV) and Cu (932.62 eV). The measurements were aligned with the adventitious carbon peak (C1s) at 284.8 eV before conducting chemical state analysis. Before the XPS test, the powder sample was placed in a crucible in the flow reactor and pretreated using the following procedure: The sample was first degreened at 750 °C for 1 h using 400 ppm NO, 8% O_2 and 5% H_2O in Ar balance, with a total flow rate of 750 mL/min, then it was pretreated at 550 °C for 30 min with 8% O_2 and 5% H_2O. The sample was thereafter exposed to 200 ppm NO_x (containing 1.8% NO_2), 0/200/400 ppm CO, 8% O_2 and 5% H_2O in Ar balance, kept at 80 °C for 45 min, and then increasing the temperature to 550 °C, with a rate of 20 °C/min and kept at 550 °C for another 15 min. After this treatment the sample was cooled down under the same feed gas, and thereafter sealed into a N_2 atmosphere to prevent re-oxidization until the XPS measurement was performed.

In-situ diffuse reflectance infrared Fourier transformed spectroscopy (DRIFTS) was conducted with a Bruker Vertex 70 spectrometer, to determine the adsorption form of NO and CO on Pd/SSZ-13. The spectrometer was equipped with an MCT detector and scanning was done at 4 cm^{-1} resolution. The sample (~20 mg) was placed into a sealed diffuse reflection chamber equipped with KBr glass windows on both sides. The sample was first degreened at 750 °C for 1 h using 400 ppm NO_x, 8% O_2 and 1% H_2O in Ar balance for 1 h, then it was pretreated at 550 °C for 30 min with 8% O_2 and 1% H_2O. After cooling the chamber down to 80 °C, the background was collected. The sample was exposed to 200 ppm NO_x, 8% O_2 and 1% H_2O in Ar for 30 min to saturate with NO adsorption, and then 400 ppm CO was introduced into the chamber with continuous scanning (1 scan/min).

2.4. Flow reactor experiments

The PNA samples were tested in a flow reactor. Detailed information about the flow reactor equipment is reported in our previous study [27]. Briefly, the monolith was placed in the quartz tube reactor and two thermocouples were respectively placed in the center of the monolith and upstream of the monolith. The inlet flow rates of gases were controlled with several mass flow controllers (Bronkhorst). Water was

evaporated via a Bronkhorst controlled evaporation and mixing system. The outlet gases were analyzed by an FTIR spectrometer (MKS Multigas 2030). The scheme of the reactor system is shown in Scheme S1.

The first PNA test involved multiple cycles using different NO_x concentrations. The total flow rate was set to 750 mL/min (i. e., 6500 h^{-1} based on the monolith volume). The sample was first degreened at 750 °C for 1 h using 400 ppm NO_x, 8% O_2 and 5% H_2O in Ar balance. Prior to all the NO_x and TPD cycles, the PNA sample was pretreated at 550 °C for 30 min with 8% O_2 and 5% H_2O. The experimental procedure for all the cycles included NO_x adsorption and TPD to represent multiple cold start periods. For cycle 1, the sample was exposed to 200 ppm NO_x, 8% O_2 and 5% H_2O in Ar balance for 45 min at 80 °C after the pretreatment. This was followed by a temperature ramp to 550 °C with a rate of 20 °C/min, while exposing the catalyst to the same gas mixture. Then the reactor was kept at 550 °C for another 15 min. After this cycle, a pretreatment for the next cycle was performed. For testing the reproducibility of the NO_x adsorption and TPD, Cycle 2 was repeated with the same inlet condition as cycle 1. For cycles 3–4 and cycles 5–6 the feed NO_x concentration was respectively set to 300 ppm and 400 ppm. Cycle 7 was then conducted with the same condition as cycles 1–2 to check the stability of the PNA sample after multi-cycle tests. It should be noted that there was a small amount of NO_2 in the NO_x gas, with a molar proportion of $NO_2/NO_x = 1.8$ mol%.

The second PNA test involved multiple cycles using different CO concentrations. The pretreatment, adsorption and TPD procedures were the same as the first PNA test except the NO_x and CO concentration in feed. The NO_x inlet concentrations in all cycles were set to 200 ppm, while the CO inlet concentration was set to 200 ppm for cycles 1–2 and 400 ppm for cycles 3–4. Cycle 5 was then conducted with the same condition as cycles 1–2 to check the stability of the PNA.

Detailed information of the procedure, gas concentrations and temperatures are summarized in Table S1.

The same procedures in first and second PNA test were conducted again for empty monolith. The NO_x profiles obtained in this empty test were further used in transient kinetic rate calculation and kinetic modeling.

The transient rate of NO_x adsorption (RNO_x) was calculated according to the following Eq. (1) [28–30]:

$$RNOx\left(molg^{-1}s^{-1}\right) = \frac{F_T}{W} y_{NOx}\left(Z^0_{NOx}(t) - Z_{NOx}(t)\right) \quad (1)$$

where F_T and W respectively represent molar flow rate and catalyst weight, Z^0_{NOX} and Z_{NOx} are dimensionless concentrations of NO_x in empty test and in evaluation, where $Z_i^*(t) = y_i(t)/y_i^f$. In this equation $y_i(t)$ is the mole fraction of NO_x at a given time and y_i^f is the mole fraction of NO_x in feed (i, e, 200/300/400 ppm).

3. Kinetic modeling

3.1. Reactor model

The kinetic modeling of the catalyst was conducted with a one-channel model using the Aftertreatment Module embedded in AVL BOOST™ software, version 2020 R2. The kinetic model was additionally used to assess the performance of a real-life sized catalyst considering spatial non-uniformities during a transient cold-start phase. For this purpose the kinetic model at hand has was plugged into a 1D catalyst model provided by the Aftertreatment Module of AVL CRUISE™ M, version 2020 R2. The material properties of thermal conductivity and specific heat capacity were adopted from the CRUISE™ M property database for cordierite material. All the nomenclature of parameters used in model description is shown in Table 1. The model contains two gas boundaries (inlet and outlet) and catalyst as elements, as shown in Scheme S1.

For the simulations in the AVL BOOST™ software for the kinetic model development, the discretization of the channel was set to 20 grid points along the axial direction. The mass-transfer inside the washcoat was modeled using five grid points. The gas species mass balance equation of the model is shown in Eq. (2)[31]:

$$\varepsilon_g \times \frac{\partial \rho_g \times w_{k,g}}{\partial t} = \varepsilon_g \times \frac{\partial \rho_g \times w_{k,g} \times v_g}{\partial z} + MG_{k,g} \sum_i^{nr} v_{i,k} \times r_i(y_k, T_s, \theta_k) \quad (2)$$

the corresponding coverage of component k on the surface was defined by Eq. (3)[28]:

$$\frac{\partial \theta_k}{\partial t}(\Theta \times GSA) = \sum_i^{nr} v_{i,k} \times r_i(y_k, T_s, \theta_k) \quad (3)$$

where GSA is the geometric surface area per unit reactor volume, which is defined by Eq. (4)[31]:

$$\frac{GSA}{d_{hyd}} = 4 \times (cell\ density) \quad (4)$$

The external mass transfer from the gas bulk to the surface of the PNA was simulated according the film model, which is defined by Eq. (5) [31]

$$GSA \times k_{k,m} \times (y_k - y_k^B) = \sum_i^{nr} v_{i,k} \times r_i(y_k, T_s, \theta_k) \quad (5)$$

A constant pore diffusion model was set for the mass transfer in the washcoat, where all the effective diffusivities of the gas components were set to $5 \times 10^{-6} m^2/s$, according to Chatterjee et al [32]. This approach has also been used in several of our previous models [33–38] for aftertreatment systems.

Owing to the low heat of reaction during the NO_x adsorption and TPD, as well as the low concentration of the reactant species, the heat balance was not solved in the kinetic model development simulations. This approach was widely used in previous models involving NO_x adsorption [33,35,37,39,40]. The reaction temperature in the model was set to the catalyst temperature measured in the monolith during the NO_x adsorption and TPD tests.

For the converter modeling, the mass transfer and heat transfer were calculated via Transport property data embedded in AVL CRUISE™ M, which comprises a list of molecular parameters for the calculation of species viscosities, thermal conductivities and diffusion coefficients of multi-component gas mixture, according to Kee R. J. et. al.[41].

Table 1
The nomenclature of parameters in model description.

Parameter	Definition	Unit
A_i	Pre-exponential factor for reaction i	s^{-1}
d_{hyd}	Hydraulic diameter of the channel	m
$E_{A,i}$	Activation energy for reaction i	J/mol
$E^0_{A,i}$	Activation energy for reaction i at zero coverage	J/mol
GSA	Geometric surface area per reactor volume	m^{-1}
$k_{k,m}$	Mass transfer coefficient of species k	mol/(m^2 s)
k_i	Rate constant for reaction i	s^{-1}
$MG_{K,G}$	Molar mass of gas phase species	kg/kmol
r_i	Reaction rate for reaction i	mol/(m^2 s)
T_s	Temperature at catalyst surface	K
t	Time	s
v_g	Gas velocity	m/s
$v_{i,k}$	Stoichiometric coefficient of species k in reaction i	–
$w_{k,g}$	Mass fraction of species k in gas phase	–
y_k	Mole fraction at the reaction layer of specie k	–
y^B_k	Mole fraction in the gas bulk of specie k	–
z	Spatial coordinate in axial direction	m
α_i	Coverage dependence in reaction i	–
ε_g	Volume fraction of gas phase in entire system	–
Θ	Site density	
θ_k	Coverage of species k	mol/m^3
ρ_g	Density of the gas phase	$kmol/m^3$
Ω_j	Surface site density of storage site j	$kmol/m^2$

3.2. Kinetic model

The reaction rate expressions were defined by ANSI C programming language embedded in the AVL User Coding Interface™. The reaction rate was calculated via the Arrhenius Equation, as shown in Eq. (6):

$$k_i = A_i e^{\frac{-E_{A,i}}{(RT_s)}} \quad (6)$$

The storage and release of NO_x on Pd sites is important for passive NO_x adsorption. It is widely accepted that the activation energy of NO_x adsorption is a non-activated step [16,42,43], and was therefore set to 0. For the NO/NO_2 desorption, a linear dependence based on coverage for the activation energy was used for Cu/ZSM-5 [42]. We used the same approach in the current work, using an activation energy for desorption determined via a Temkin isotherm, as shown in Eq. (7):

$$E_{NO_x,des} = E^0_{NO_x,des}(1 - \alpha\theta_{NO_x}) \quad (7)$$

4. Results and discussion

4.1. Catalyst characterization of Pd/SSZ-13

It has been reported that Pd/SSZ-13 is adequate for passive adsorption of NO_x owing to its considerable NO_x adsorption ability, H_2O and sulfur resistance [10,13,44]. Thus Pd/SSZ-13 with a Pd loading of ~ 1% was synthesized and used for NO_x adsorption and TPD. The properties of the as-prepared Pd/SSZ-13 were determined via several characterization methods. The measured Pd loading was 0.98% and the Si/Al ratio was 12.0. The specific surface area and pore volume of Pd/SSZ-13 were 659 $m^2\ g^{-1}$ and 0.30 $cm^3\ g^{-1}$ respectively, which were calculated from a N_2 adsorption–desorption isotherm. The XRD pattern of Pd/SSZ-13 is shown in Figure S1. All the peaks could be attributed to the SSZ-13 zeolite. The absence of peaks from palladium oxide species was mainly due to the low Pd loading and high Pd dispersion.

ESEM-EDS was conducted to measure the thickness of the washcoat, as shown in the EDS mapping in Figure S2. The clear Al and Si signals of the zeolite assisted in distinguishing the washcoat from the cordierite. Compared to Pd/SSZ-13 washcoat, the cordierite structure contains more Al but less Si, leading to the clear contrast between washcoat and monolith. It could be measured from Figure S2 that the washcoat thickness of the monolith sample was 70 ± 40 μm.

4.2. NO_x adsorption and TPD on Pd/SSZ-13

We first evaluated the Pd/SSZ-13 sample for NO_x passive adsorption without the presence of CO (i.e., 200–400 ppm NO_x/ 8% O_2/ 5% H_2O/ balance Ar). Before evaluation, a degreening procedure was conducted at 750 °C for the as-prepared Pd/SSZ-13 sample in order to increase the amount of ion-exchanged Pd species [44]. To describe multiple cold start periods, the sample was tested with multi-cycle passive NO_x adsorption and release, including a pretreatment procedure with O_2 and H_2O between each cycle. The detailed procedure is shown in Table S1. The NO_x adsorption and release cycle was repeated in each conditions to test the reproducibility, as shown in Figure S3. A comparison of NO and NO_2 profiles between cycle 2 and cycle 7 (repeated experiments) are shown in Figure S4, demonstrating that there is no deactivation of Pd/SSZ-13 during multi-cycle tests using the examined inlet gas feed. It could be inferred from the result that the Pd/SSZ-13 was completely regenerated between the cycles. Therefore, the profiles of all the cycles could be analyzed separately. Cycle 2, cycle 4 and cycle 6 were chosen to evaluate the result with 200 ppm, 300 ppm and 400 ppm inlet NO, respectively. The concentration of outlet NO, NO_2 and NO_x as well as reaction temperature are shown as the function of time on steam in Fig. 1.

The adsorption branch at 80 °C during the first 45 min in Fig. 1A demonstrates that the outlet NO concentration becomes stable after around 1500 ~ 2000 s, indicating that saturation of NO was reached. The NO_2 profiles are shown in Figure S5 and it should be noted that the NO_2 concentrations are below 5 ppm during the NO adsorption for all NO concentrations. Owing to the sudden opening of the mass flow controllers initially in the NO adsorption, there were some overshoots of NO concentration in inlet gas, which is therefore also observed in the outlet NO signal. The transient rate of NO_x adsorption was further calculated as shown in Figure S6. It could be seen that with increased NO_x concentration, the transient NO_x adsorption rate was increased. After 2700 s, the temperature started to increase to 550 °C with a rate of 20 °C/min, and several NO_x desorption peaks were found. There is one NO consumption peak at 166 °C observed and two NO desorption peaks at 252 °C and 371 °C, respectively, while the NO_2 desorption peak only appears at 166 °C. Based on the desorption profiles we suggest that these peaks could be attributed to three different Pd sites, which is clearer in the NO_x profile as shown in Fig. 1B. After the temperature reached 550 °C (~4100 s), NO was partially oxidized by O_2 and produced NO_2, while there is no NO or NO_2 released from Pd sites due to the same NO_x concentration in inlet and outlet. Thus, some NO oxidation occurred over the sample. Note that empty reactor tests were performed to ensure that the NO oxidation occurred over the catalyst. It should be pointed out that the first NO_x desorption peak is at 166 °C, a temperature which is ineffective for urea dosing and subsequent SCR treatment, while the

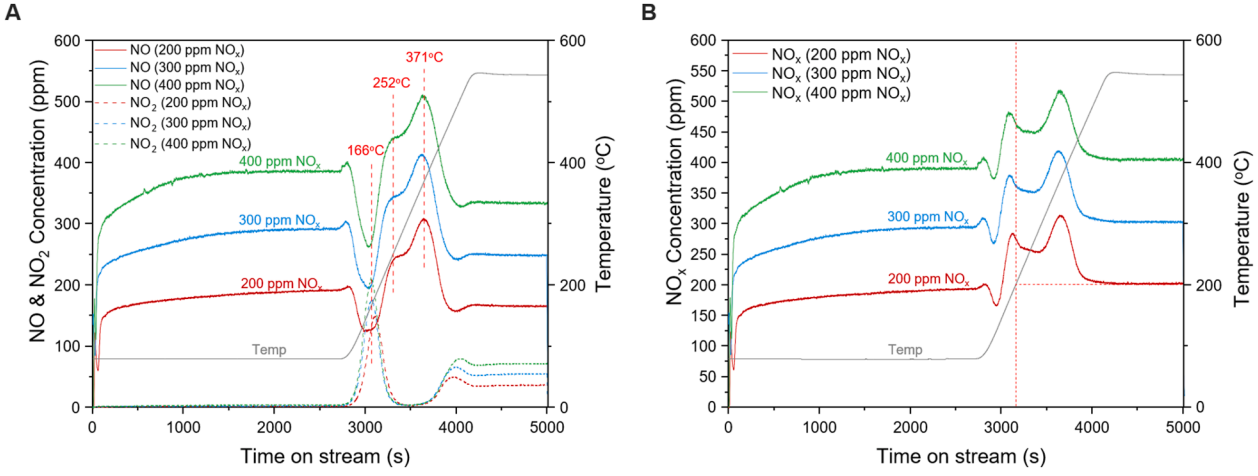

Fig. 1. NO & NO_2 profiles (A) and NO_x (B) profiles for NO_x adsorption & TPD with different concentration of NO_x in inlet. Reaction conditions: 200/300/400 ppm NO_x (containing 1.8% NO_2), 5% H_2O, 8% O_2 in Ar with the flow rate of 750 mL/min. The data were selected from cycle 2 (200 ppm), cycle 4 (300 ppm), cycle 6 (400 ppm) respectively.

other two NOx desorption peaks are above the minimum urea dosing temperature.

The NO_x/Pd ratio was also calculated based on the Pd loading and NO_x transient adsorption and desorption branch, as shown in Table 2. It could be seen that the NO_x/Pd ratio for different inlet NO_x concentrations is 0.61 ~ 0.68, indicating that the Pd sites were saturated by NO_x during the adsorption using a gas condition of 200 ppm NO_x. It is also reported in previous works that the NO_x/Pd ratio on Pd/SSZ-13 under the existence of H_2O is around 0.45 ~ 0.78 [16,23]. Owing to the suppression of H_2O on NO_x adsorption the NO_x/Pd ratios are<1. The NO_x/Pd was also influenced by the dispersion of PdO clusters. Furthermore, it could be seen the NO_x/Pd was similar in transient adsorption branch and in desorption branch, indicating that all the absorbed NO_x species were eventually released in the TPD process. The different adsorbed NO_x species from different inlet NO_x concentrations released at the same temperature, indicating the adsorption sites or active sites are less affected by NO_x concentration.

4.3. Kinetic model for passive NO_x adsorption over Pd/SSZ-13

Based on the NO_x adsorption and TPD profile from Pd/SSZ-13, we developed a multi-site kinetic model to describe the mechanism of passive NO_x adsorption. The reaction steps are shown in Table 3, with the corresponding parameters in Table S2. It is widely accepted in previous works that Pd^{2+} cation sites are responsible for NO_x adsorption in Pd supported zeolites [8,12,45]. The Pd^{2+} cations can bind to two Al ($Z^-Pd(II)Z^-$) or only one Al and be charge balanced by an OH group ($Z^-[Pd(II)OH]^+$) [13,17,20]. Therefore, we use $Z^-Pd(II)Z^-$ and $Z^-[Pd(II)OH]^+$ as initial sites on Pd/SSZ-13, which is also consistent with our previous work [15]. The NO can adsorb on these sites at 80 °C during the NO_x adsorption branch. These reactions are described by reactions R1 and R3. Note that the NO_x/Pd (as listed Table 2) is lower than 1, thus multiple NO adsorption on a single site is not considered. Furthermore, due to the small amount of NO_2 in the inlet gas, NO_2 adsorption on $Z^-Pd(II)Z^-$ was also considered (reaction R2). The interaction between NO and Pd^{2+} cation sites have previously been investigated by Mei et al. and Ambast et al [16,20]. using density functional theory (DFT) simulations. They found that the binding energy of $Z^-Pd(II)Z^-NO$ is much higher than that of $Z^-[Pd(II)OH]^+$-NO[16,20]. Furthermore, the activation barrier of $Z^-[Pd(II)OH]^+$ reduction by NO is only half of that of $Z^-Pd(II)Z^-$ reduction [20]. Therefore, it could be deduced that the $Z^-[Pd(II)OH]^+$ site is easily reduced by adsorbed NO species to form $Z^-Pd(I)^-$ when the temperature increases, as described in reaction R4. The reduced site $Z^-Pd(I)^-$ shows the highest NO stability after adsorption (reaction R5) among all the $Pd^{2+/}Pd^+$ cation sites[16,17,20]. Therefore, according to the results in Fig. 1A, the NO desorption peaks at 252 °C and 371 °C were assigned to the NO desorption on $Z^-Pd(II)Z^-$ and $Z^-Pd(I)^-$, respectively. Accordingly, the NO consumption peak and the corresponding NO_2 formation peak in the beginning of temperature ramp (166 °C) could be described by the reduction of $Z^-[Pd(II)OH]^+$. Furthermore, it has been demonstrated that the Pd/SSZ-13 sample was not deactivated after a multi-cycle test as in Figure S4, which indicates that the initial sites ($Z^-Pd(II)Z^-$ and $Z^-[Pd(II)OH]^+$) should return to their original form after the pretreatment. Therefore, in the pretreatment procedure prior to the next-cycle, $Z^-Pd(I)^-$ sites are re-oxidized back to the initial $Z^-[Pd(II)OH]^+$ sites (reaction R6) under the inlet-gas condition containing only O_2 and H_2O.

Table 2
NO_x/Pd calculated from NO_x profiles in Fig. 1.

NO_x in feed (ppm)	NO_x/Pd-ad.[a]	NO_x/Pd-de.[b]
200	0.61	0.64
300	0.65	0.67
400	0.68	0.64

[a] Calculated from transient adsorption branch
[b] Calculated from desorption branch

Table 3
Reaction Mechanism for passive NO_x adsorption on Pd/SSZ-13.

Reaction	Reaction Step	Rate formation
R1	$Z^-Pd(II)Z^-+NO \rightleftharpoons Z^-Pd(II)Z-NO$	$r_1 = k_{1f}\Psi_1\theta_{S1}y_{NO} - k_{1b}\Psi_1\theta_{S1\text{-}NO}$
R2	$Z^-Pd(II)Z^-+NO_2 \rightleftharpoons Z^-Pd(II)Z^--NO_2$	$r_2 = k_{2f}\Psi_1\theta_{S1}y_{NO2} - k_{2b}\Psi_1\theta_{S1\text{-}NO2}$
R3	$Z^-[Pd(II)OH]^+ + NO \rightleftharpoons Z^-[Pd(II)OH]^+ - NO$	$r_3 = k_{3f}\Psi_2\theta_{S21}y_{NO} - k_{3b}\Psi_2\theta_{S21\text{-}NO}$
R4	$2Z^-[Pd(II)OH]^+ - NO \rightleftharpoons Z^-Pd(I) + Z^-Pd(I) - NO + NO_2 + H_2O$	$r_4 = k_{4f}(\Psi_2\theta_{S21\text{-}NO})^2 - k_{4b}\Psi_2\theta_{S22}\Psi_2\theta_{S22\text{-}NO}y_{NO2}y_{H2O}$
R5	$Z^-Pd(I) + NO \rightleftharpoons Z^-Pd(I) - NO$	$r_5 = k_{5f}\Psi_2\theta_{S22}y_{NO} - k_{5b}\Psi_2\theta_{S22\text{-}NO}$
R6	$2Z^-Pd(I) + H_2O + 0.5O_2 \rightleftharpoons 2Z^-[Pd(II)OH]^+$	$r_6 = k_{6f}(\Psi_2\theta_{S22})^2y_{H2O}y_{O2}{}^{0.5} - k_{6b}(\Psi_2\theta_{S21})^2$
R7	$Pd(II)O + 2NO + 1.5O_2 \rightleftharpoons Pd(NO_3)_2$	$r_7 = k_{7f}\Psi_3\theta_{S31}y_{NO}{}^2y_{O2}{}^{1.5} - k_{7b}\Psi_3\theta_{S32}$
R8	$Pd(NO_3)_2 + NO \rightleftharpoons Pd(II)O + 3NO_2$	$r_8 = k_{8f}\Psi_3\theta_{S32}y_{NO} - k_{8b}\Psi_3\theta_{S31}y_{NO}{}^3$
R9	$2NO + O_2 \rightleftharpoons 2NO_2$	$r_9 = k_{9f}y_{NO}{}^2y_{O2} - k_{9b}y_{NO2}{}^2$
Thermodynamic restriction		
Reactions	Overall reaction	Restriction on parameters
2R3 + R4-R5 + R6	$NO + 0.5O_2 \rightleftharpoons NO_2$	$\Delta H_{NOox} = 2[E_{f3}\text{-}E_{b3}(1\text{-}\alpha_{b3}\theta_{S3NO})] + (E_{f4}\text{-}E_{b4}) - [E_{f5}\text{-}E_{b5}(1\text{-}\alpha_{b5}\theta_{S4NO})] + (E_{f6}\text{-}E_{b6})\Delta S_{NOox} = 2Rln(A_{f3}/A_{b3}) + Rln(A_{f4}/A_{b4}) - Rln(A_{f5}/A_{b5}) + Rln(A_{f6}/A_{b6})$
R7 + R8	$3NO + 1.5O_2 \rightleftharpoons 3NO_2$	$\Delta H_{NOox} = (E_{f7}\text{-}E_{b7}) + (E_{f8}\text{-}E_{b8})\Delta S_{NOox} = Rln(A_{f7}/A_{b7}) + Rln(A_{f8}/A_{b8})$

Storage sites:Ψ1:ZPd; Ψ2:ZPdOH; Ψ3:PdO
Storage species: S1: $Z^-Pd(II)Z^-$ S21: $Z^-[Pd(II)OH]^+$ S22: $Z^-Pd(I)$ S31: Pd(II)O S32: $Pd(NO_3)_2$

The steps involving NO and NO_2 adsorption are assumed to be non-activated, thus the activation energy of them are set to 0. The activation barriers of some reactions on Pd/ZSM-5,Pd/BEA and Pd/SSZ-13 were investigated by DFT studies [16,20], and these values are used in the current model after slight tuning. Moreover, the reactions occurring on $Z^-[Pd(II)OH]^+$ sites (Reactions R3-R6) must meet the thermodynamic restriction for the overall NO oxidation, as shown in Table 3.

The reactions occurring on $Z^-Pd(II)Z^-$ sites (R1, R2) and $Z^-[Pd(II)OH]^+$ sites (R3-R6) were first modeled separately, as shown in Fig. 2A and 2B respectively. The storage capacity of these two sites was tuned to 2 mol/m^3 ($Z^-Pd(II)Z^-$) and 2.2 mol/m^3 ($Z^-[Pd(II)OH]^+$) based on converter volume. However, it was found in Fig. 2B that the NO consumption peak and NO_2 generation peak at 166 °C are much smaller than the those in experiments, while the NO desorption peak attributed to $Z^-Pd(I)^-$- NO at 371 °C matched well with the experimental profile. This result demonstrates that there are also other reactions which consume NO and generate NO_2 around 166 °C. During the synthesis of Pd/SSZ-13 via the impregnation method, there are a small amount of PdO species also generated outside the framework of SSZ-13, in the form of nanoparticles or clusters [12,15]. These PdO species provide for a low NO adsorption amount owing to the limited number of exposed surface sites. In order to describe this feature, reactions R7 and R8 were added where PdO species react with NO in the presence of O_2 to form $Pd(NO_3)_2$ (reaction R7), which subsequently decomposes back to PdO species with NO_2 release (reaction R8) [12,15,46]. The storage capacity of PdO sites was tuned to 1.7 mol/m^3 based on the converter volume. Herein, it could be deduced that the formation and decomposition of $Pd(NO_3)_2$ also occurred at ~ 166 °C in the NO_x adsorption and TPD test. Based on this mechanism, simulation of adsorption on PdO sites only was also conducted and is shown in Fig. 2C. Notably, the reactions occurring on the PdO site (R7, R8) also must meet the thermodynamic restrictions for NO oxidation, as shown in Table 3.

Based on the reaction mechanisms on the three sites ($Z^-Pd(II)Z^-$, $Z^-[Pd(II)OH]^+$ and PdO), the overall simulation was conducted as shown in Fig. 2D. NO oxidation can occur through reactions (R3-R6). However,

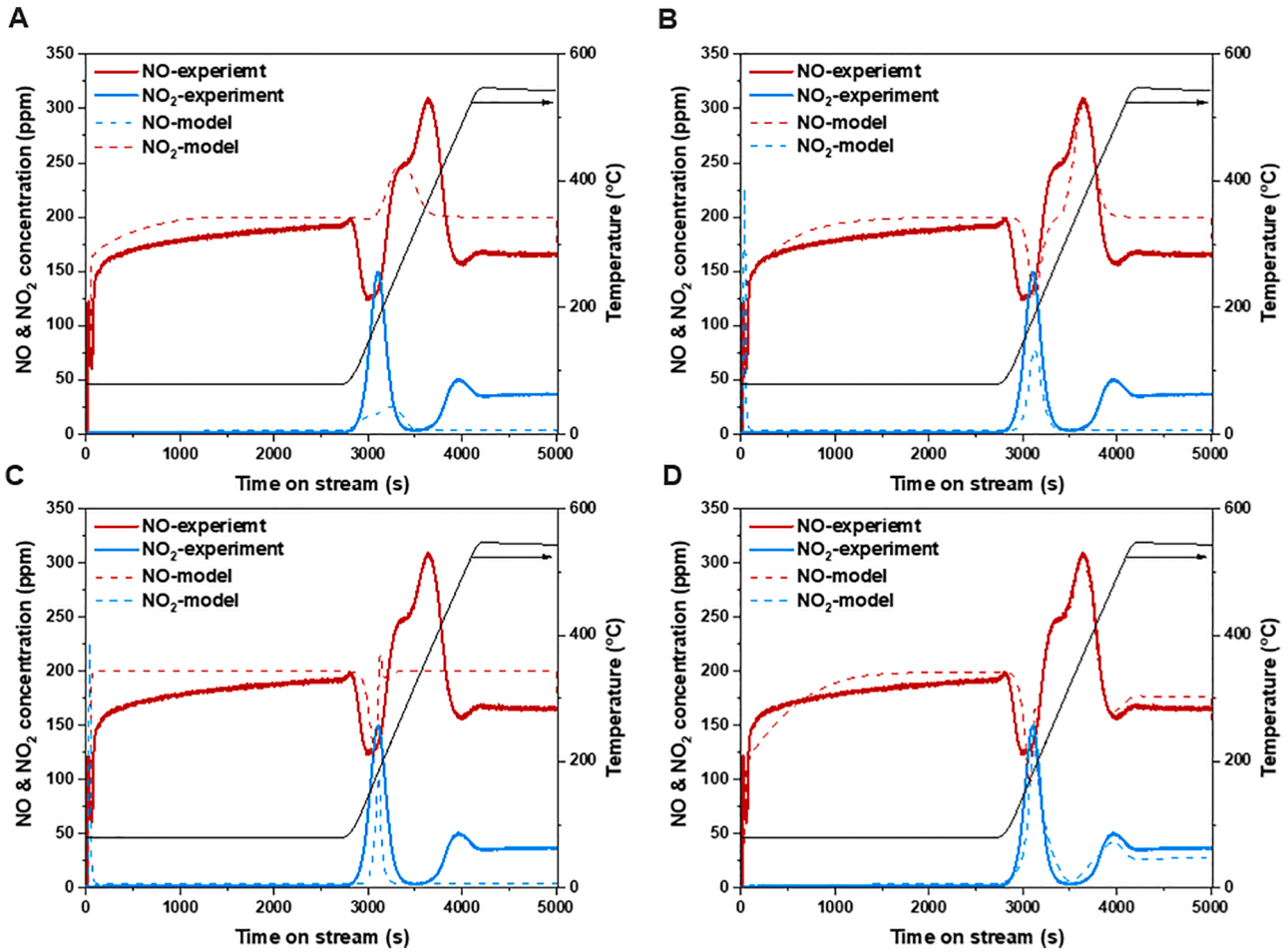

Fig. 2. Kinetic modeling of the contribution of each individual Pd site according to: A: Z⁻Pd(II)Z⁻, B: Z⁻[Pd(II)OH]$^+$, C: PdO; D: Overall modeling of all three Pd sites.

these reactions were not enough to describe the continuous NO oxidation occurring at high temperature. In order not to further complicate the model we added one global reaction step (R9) to describe the continuous NO oxidation. The agreement between experimental data and predicted model are satisfactory in both NO and NO_2 concentration, as shown in Fig. 2D. A more detailed examination of the process can be done by the model-predicted coverages of Pd species during the NO_x adsorption and TPD (Fig. 3). The coverages of NO and NO_2 adsorbed on Z⁻Pd(II)Z⁻ were gradually increasing in the beginning of adsorption branch and all Z⁻Pd(II)Z⁻ sites were occupied after ~ 1500 s (Fig. 3A). When the temperature started to increase, adsorbed NO_2 and NO released successively, leaving 100% empty Z⁻Pd(II)Z⁻ sites at high temperature.

The model-predicted coverages on Z⁻[Pd(II)OH]$^+$ is more complicated as shown in Fig. 3B. Z⁻[Pd(II)OH]$^+$ first absorb NO in the beginning of the adsorption branch to from Z⁻[Pd(II)OH]$^+$ – NO, accompanied by a low percentage (7%) of reduction to Z⁻Pd(I)⁻ – NO. With increasing temperature, two Z⁻[Pd(II)OH]$^+$ –NO sites were reduced by one of the absorbed NO to form Z⁻Pd(I)⁻ –NO and Z⁻Pd(I)⁻ (reaction R4). Subsequently the empty Z⁻Pd(I)⁻ absorbed NO immediately to form another Z⁻Pd(I)⁻ –NO. NO was released from Z⁻Pd(I)⁻ when the temperature increased to 371 °C (~3600 s), resulting in 100% empty Z⁻Pd(I)⁻ sites in the following TPD. Furthermore, a long-term modeling including NO adsorption, TPD and pretreatment procedures was simulated as shown in Figure S7. It could be seen that Z⁻Pd(I)⁻ reacts with O_2 and H_2O after the inlet NO was turned off, leading to 100% Z⁻[Pd(II)OH]$^+$ at the end of pretreatment. Thus, returning all Pd species back to their original states.

The model-predicted changes of PdO species during the NO_x

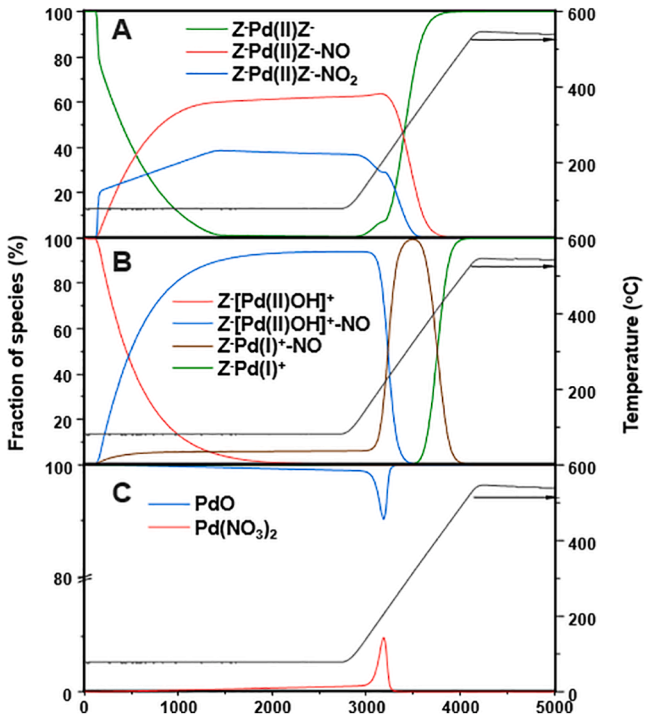

Fig. 3. Model-predicted coverage (mean values) of different species on sites A: Z⁻Pd(II)Z⁻, B: Z⁻[Pd(II)OH]$^+$ and C: PdO.

adsorption and TPD is showed in Fig. 3C. It could be seen that the NO adsorption on PdO is very slow, in accordance with previous works [15,46]. More PdO converted to $Pd(NO_3)_2$ when temperature started to increase. Shortly after the start of the temperature ramp, the dissociation rate of $Pd(NO_3)_2$ exceeded the formation rate, resulting in the re-generation of PdO.

The model was further verified by PNA multi-cycle tests with different inlet NO_x concentrations, the procedure of which is shown in Table S1 (test 1, cycle 1–6). Fig. 4A shows the inlet NO_x concentration and reaction temperature, and Fig. 4B shows the outlet NO & NO_2 concentration from the model and experiment. Moreover, magnified results of cycle 2, cycle 4 and cycle 6 are shown in Fig. 5. The model well describes the multi-cycle test including the NO and NO_2 outlet with different NO_x concentrations in the feed. The initial Pd sites ($Z^-Pd(II)Z^-$, $Z^-[Pd(II)OH]^+$ and PdO) were all returned to their original states in the end of every cycle, indicating there is no deactivation of Pd/SSZ-13 during multi-cycle test, which is in accordance with the experimental results presented in Figure S4.

4.4. CO assisted NO_x adsorption and TPD on Pd/SSZ-13

The effect of CO on passive NO_x adsorption was further investigated in this work. A multi-cycle test of Pd/SSZ-13 with 200 ~ 400 ppm inlet CO was conducted with the procedure including pretreatment, NO_x adsorption and TPD, same as the multi-cycle test without CO in Section 4.3. The detailed procedure is shown in Table S1, test 2. During the NO_x adsorption and TPD process, the inlet gas composition (200/400 ppm CO, 200 ppm NO, 5% O_2, 7% H_2O balanced in Ar) was constant. Previous work reported that high CO concentrations may deactivate the supported metal catalyst by inducing agglomeration or blocking of the active sites [22,44]. To check the deactivation in our case, with low CO concentrations, cycle 5 was conducted using the same condition as cycle 1, 2 after the multi-cycle test. No obvious change could be found between the cycle 2 and cycle 5 profiles as shown in Figure S8, indicating that there is also no deactivation for Pd/SSZ-13 in the presence of 200 ~ 400 ppm CO during the number of cycles examined in this work. Accordingly, the NO and NO_2 profiles of all the cycles could also be analyzed separately. Cycle 2 and cycle 4 were chosen to respectively represent the evaluation data with 200 ppm and 400 ppm inlet CO, while the profile of cycle 2 in test 1 was chosen as the data without CO. The concentration of outlet NO, NO_2 and NO_x as well as the reaction temperature are shown as a function of time on stream in Fig. 6. Although there was CO present in the feed, only trace amount of N_2O (<0.2 ppm) was detected during the NO_x adsorption and TPD procedure. This is because the high activation barrier of CO oxidation by NO (177 kJ/mol) [47]. Under excessive O_2, the reaction between CO and NO was intensively suppressed.

It could be seen from the adsorption branch in Fig. 6A that saturation with NO adsorption was reached at ~ 1000 s. The transient NO_x adsorption rate was further calculated as shown in Figure S9. After adding CO, the time point that NO_x adsorption rate reaches to maximum was delayed, and it did not increase compared to the rate without CO. Comparing the desorption peaks without CO addition, the position of the three peaks were the same (166 °C, 252 °C and 371 °C) as with CO addition, whereas the area of all the peaks are considerably changed. The NO_2 peak at 166 °C was markedly decreased, resulting in that the reduction of $Z^-[Pd(II)OH]^+$ and PdO by NO was suppressed. It could be further deduced that these two Pd sites may be reduced by CO instead of NO, in accordance with previous works [12,48]. The NO desorption peak at 371 °C was increased using 200 ppm CO but decreased back when the CO concentration increased to 400 ppm. On the contrary, the NO desorption peak at 252 °C was increased using 400 ppm CO. Furthermore, at higher temperature, NO oxidation to continuously produce NO_2 also occurred in the presence of CO. The NO_x profiles with 0–400 ppm CO are shown in Fig. 6B. After adding CO into the feed gas, all the NO_x was released above 200 °C, which is beneficial since it is above the temperature that urea can be dosed for downstream SCR system. The calculated NO_x/Pd ratio is shown in Table 4, demonstrating the NO_x/Pd ratio with CO feed is almost the same as that without CO, and absorbed NOx species were completely released in the TPD process. This is consistent with the result in Table 2, that indicated the Pd sites are saturated with 200 ppm NO, and the multi-species adsorption is strongly suppressed by H_2O. Based on these results, it could be concluded that the presence of CO with 200 ~ 400 ppm has a positive effect by increasing the release temperature of NO_x, instead of promoting the NO_x adsorption amount over Pd/SSZ-13.

Although it is widely accepted the presence of low CO concentration assists the passive NO_x adsorption, the role of CO is still being debating

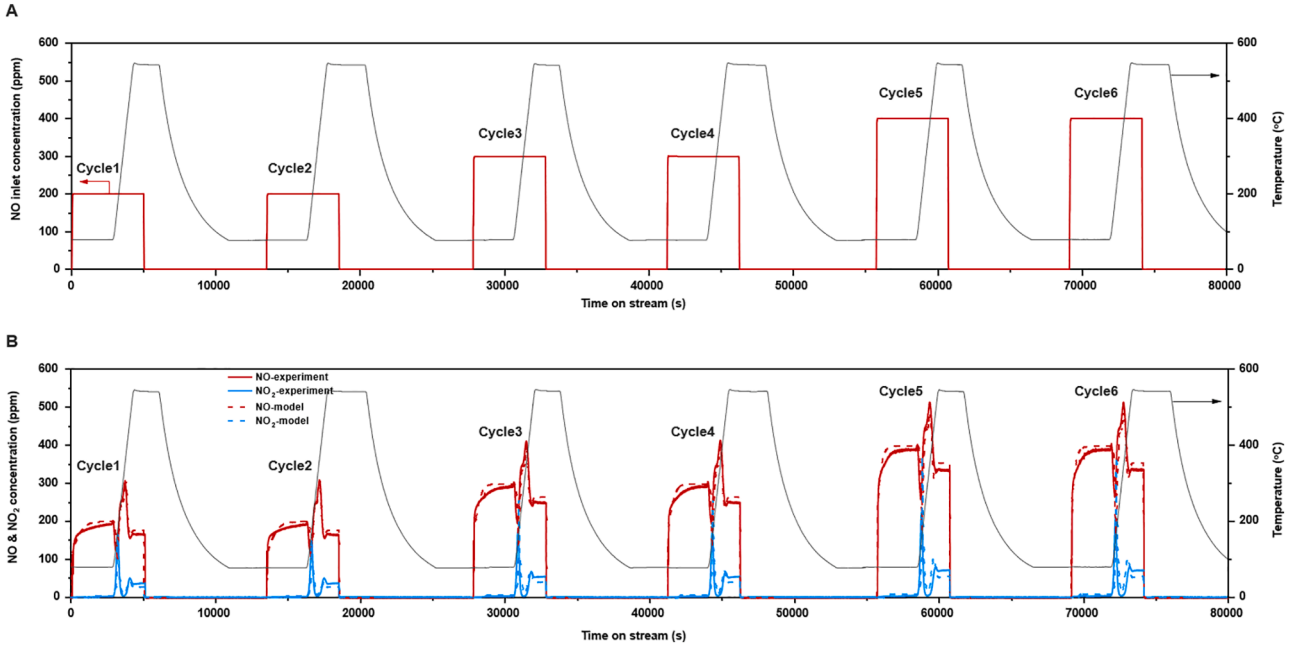

Fig. 4. Multi-cycle experimental and modeling results with different inlet NO_x concentration. A: Inlet NO_x concentration and temperature. B: NO & NO_2 concentration in experiment and modeling. Reaction conditions: NO_2/NO_x = 1.8%, 5% H_2O, 8% O_2 in Ar with the flow rate of 750 mL/min.

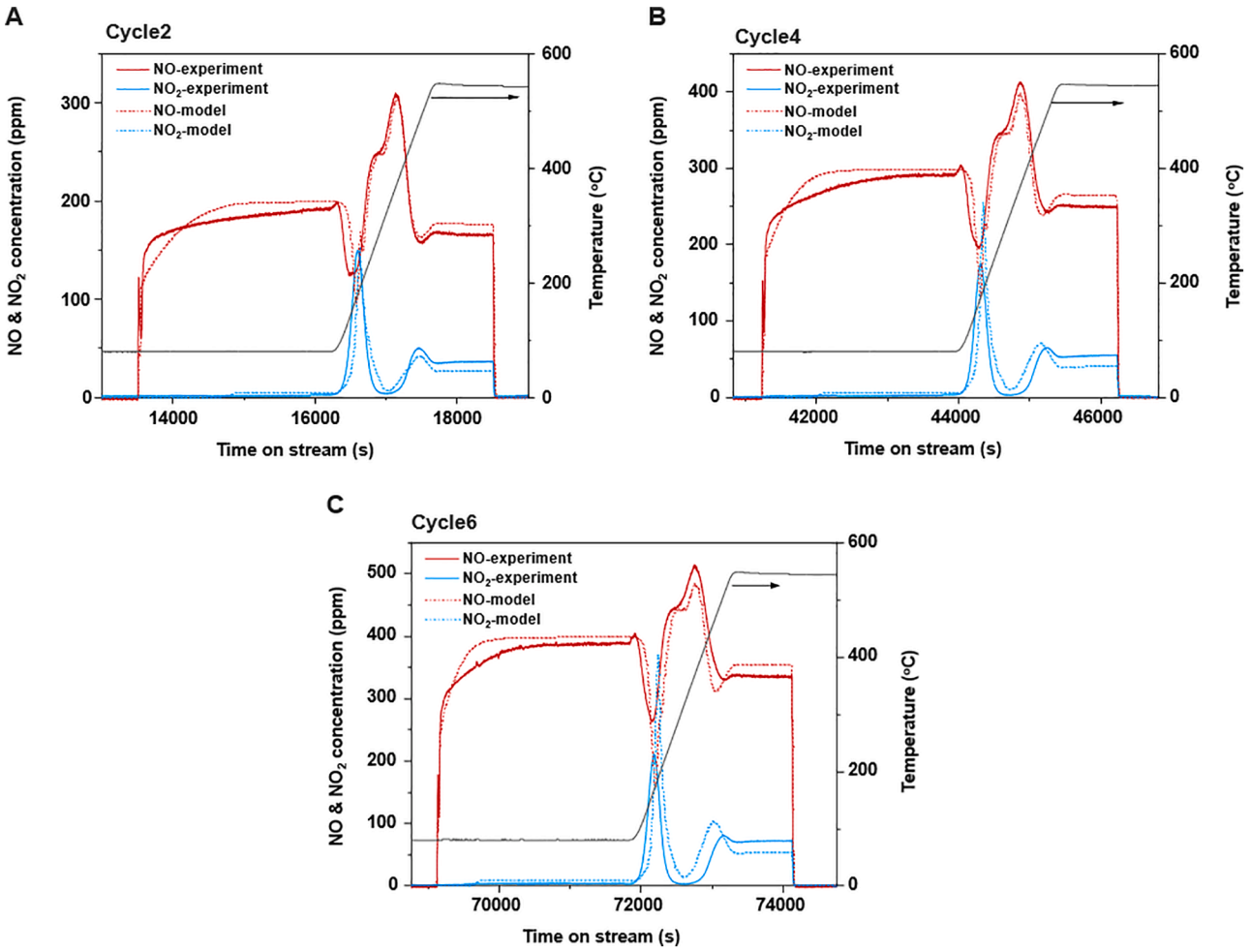

Fig. 5. Magnified results of cycle 2, 4, 6 with different inlet NO_x concentration. Reaction conditions: 200 ppm NO_x (A)/ 300 ppm NO_x (B)/ 400 ppm NO_x (C), NO_2/NO_x = 1.8%, 5% H_2O, 8% O_2 in Ar with the flow rate of 750 mL/min.

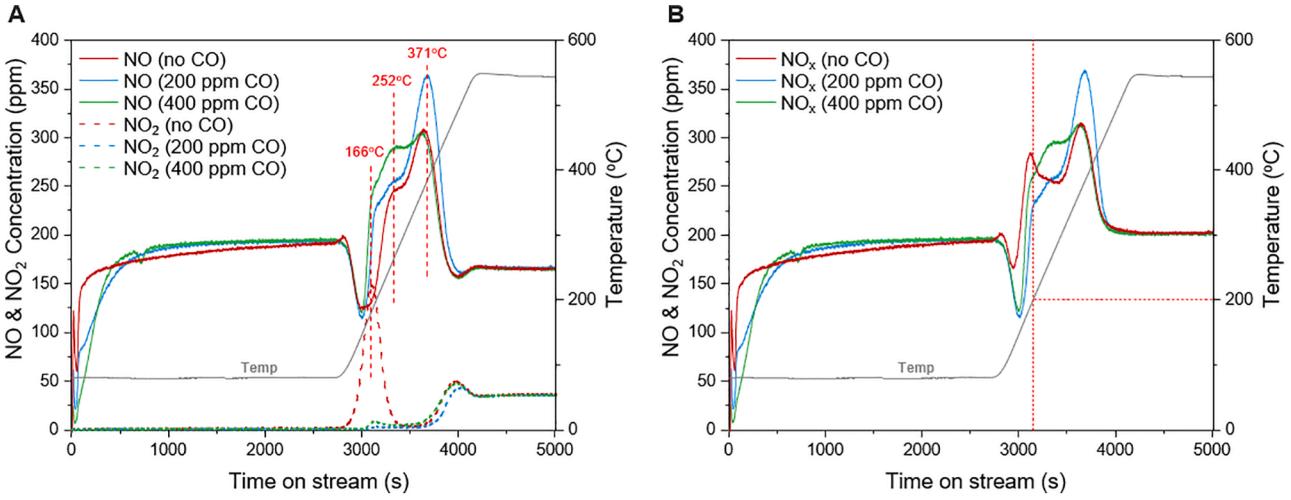

Fig. 6. NO & NO_2 profiles (A) and NO_x (B) profiles in NO_x adsorption & desorption with different concentration of CO in the inlet. Reaction conditions: 200 ppm NO, 0/200/400 ppm CO, 5 % H_2O, 8 % O_2 in Ar with the flow rate of 750 mL/min.

in recent works [12,13,18,19]. There are two possibilities suggested: (1) CO induces the formation of co-adsorbed Pd(II)(NO)(CO) species, and consequently enhances the NO_x storage [13,18,49]; (2) Pd species reduced by CO show a more efficient ability in NO_x adsorption [8,12,20]. We here first assess these two possibilities for our Pd/SSZ-13 with our used reaction conditions as a prerequisite for updating the PNA model with the addition of CO. To understand the (CO)(NO) co-adsorption as well as its influence on NO_x adsorption, the CO + CO_2 (CO_x) concentration profile during the NO_x adsorption and TPD processes was plotted as shown in Fig. 7. It should be noted that the sudden

Table 4
NO_x/Pd calculated from NO_x profiles in Fig. 6.

CO in feed (ppm)	NO_x/Pd-ad.[a]	NO_x/Pd-de.[b]
0	0.61	0.64
200	0.67	0.69
400	0.64	0.68

[a] Calculated from transient adsorption branch
[b] Calculated from desorption branch

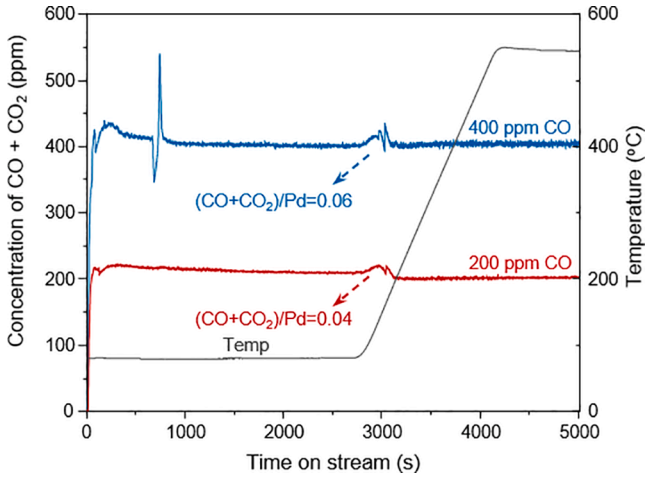

Fig. 7. CO + CO_2 and the corresponding temperature profiles. The calculated (CO + CO_2)/Pd is also given.

spike around 800 s for the 400 ppm case is due to water condensation and evaporation. It could be seen the CO_x concentration immediately reached the inlet CO concentration in the beginning of the adsorption branch, indicating that there is only minor CO adsorption on Pd/SSZ-13. This result is more obvious in the desorption branch where there is only a small CO_x desorption peak in the beginning of the temperature ramping (160 °C, ~3000 s). Compared to the NO_x/Pd ratio (0.64 ~ 0.69), the calculated CO_x/Pd (0.04 ~ 0.06) was extremely low. With careful consideration, even if a small amount of CO is absorbed during the NO_x adsorption, it still could not explain the large differences observed experimentally between the experiments in the presence and absence of CO. Moreover, all CO_x was released below 200 °C (Fig. 7) and the CO effect was observed also above this temperature.

Adsorption of NO and CO on Pd/SSZ-13 at 80 °C was further determined by in situ DRIFTS under the presence of 1% H_2O and 8% O_2, as shown in Fig. 8. The bands around 1319–1452 cm^{-1} were attributed to Pd nitrate and nitrite species[18]. The bands at 1865 cm^{-1} can be attributed to Pd^{2+}–NO according to Gupta et al.[21] and Khivantsev et al.[13]. We also find a peak at 1813 cm^{-1} and peaks in this region (1805 cm^{-1}[13,21] and 1810 cm^{-1}[50]) has previously been assigned to Pd^{+}–NO for Pd/SSZ-13.

It could be seen that most of Pd^{2+} cations were reduced even at 80 °C. Furthermore, the peaks at 1950 cm^{-1} and 2146 cm^{-1} resulted from $Pd^{\delta+}$–CO vibrations [13,18]. Compared to the NO adsorption peaks, the CO adsorption peaks were much lower, verifying the fact that there is only minor CO adsorption on Pd/SSZ-13. Based on the CO_x desorption amount in Fig. 7 and DRIFTS in Fig. 8, it could be deduced that formation of Pd(II)(NO)(CO) species is likely not the main reason for the different stability of the NO_x species in our experiments.

To further examine the other possibility that Pd species were reduced by CO which influenced the NO_x adsorption strength, Pd species treated under different CO concentrations were further investigated by XPS. Degreened Pd/SSZ-13 powder samples were first treated according to the NO_x adsorption and TPD test procedure with different CO concentrations (i.e, the procedures of cycle 2 in test 1, cycle 2 and 4 in test 2 as

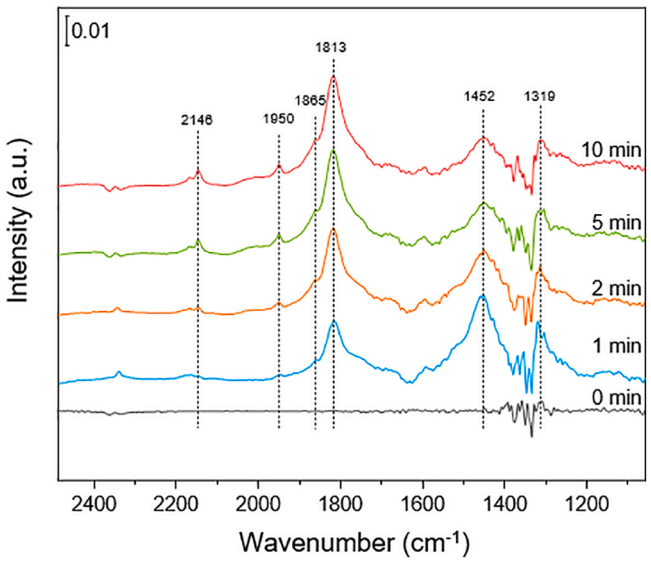

Fig. 8. DRIFTS spectra obtained during exposure to 200 ppm NO, 400 ppm CO, 1% H_2O and 8% O_2 at 80 °C with Pd/SSZ-13.

shown in Table S1). The XPS spectra of these samples are shown in Fig. 9. The peak positions of Pd(II) and Pd(I) were close [12,51–53], and it is difficult to deconvolute peaks that are close with high accuracy. We therefore instead only analyzed the XPS peak using Pd(II)($E_b(Pd3d_{5/2})$ = 337.6 eV, $E_b(Pd3d_{3/2})$ = 342.8 eV) and Pd^0 ($E_b(Pd3d_{5/2})$ = 335.9 eV, $E_b(Pd3d_{3/2})$ = 340.6 eV) reference peaks [51–53], to get information about the degree of reduction. But of course, there will also be some Pd (I) species, and thus the amounts of Pd^{II} and Pd^0 should not be viewed as absolute numbers, but instead used for comparing the reduction degree between different samples. It could be seen from Fig. 9 that there is no Pd^0 in the absence of CO, while there is respectively 14% and 59% of Pd^0 sites after experiments with 200 ppm and 400 ppm CO, respectively. These results strongly demonstrate that CO facilitates the reduction of Pd sites during passive NO_x adsorption. Meanwhile, the absence of the

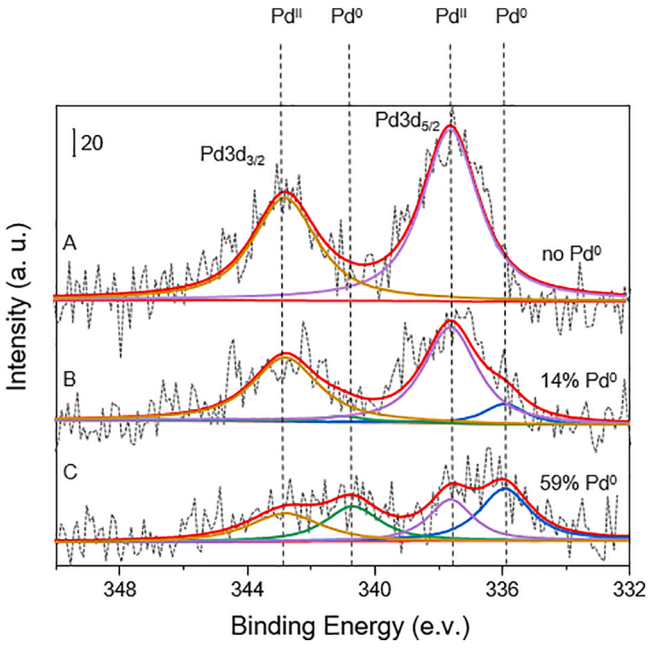

Fig. 9. Pd 3d XPS spectra for the Pd/SSZ-13 samples treated in 550 °C under A: 200 ppm NO, 5 % H_2O, 8 % O_2 in Ar; B: 200 ppm NO, 200 ppm CO, 5 % H_2O, 8 % O_2 in Ar; C: 200 ppm NO, 400 ppm CO, 5 % H_2O, 8 % O_2 in Ar.

NO_2 peak in Fig. 6A with the existence of CO could also further support that the Pd species was reduced by CO instead of NO. It is reported that the reduced metallic Pd cluster shows a strong interaction towards NO species [54,55] with a binding energy of 220 ~ 250 kJ/mol, which is similar to that of $Z^-Pd(I)^+$ sites (245 kJ/mol). Furthermore, the Pd^0 site in the zeolite is also reported to strongly absorb NO_x species [20]. Accordingly, it is deduced that in our experiments it is the Pd species reduced by CO that increase the stability of the adsorbed NO_x species.

4.5. Kinetic model for CO assisted passive NO_x adsorption

Based on the experimental results described in Section 4.4 for CO assisted NO adsorption and TPD on Pd/SSZ-13, we included new reaction steps for CO in the multi-site kinetic model described in Table 3. The additional reactions are shown in Table 5, with the corresponding parameters in Table S2. The main mechanism for the influence of CO is the reduction of the Pd sites as it was observed in the XPS analysis (Section 4.4). Z^-H^+-Pd(0) and metallic Pd, which are respectively formed from reduction of $2Z^-Pd(I)^+$ and PdO, were therefore included in the model.

The results in Fig. 6A show that the NO_2 desorption peak is absent, and this suggests that the reactions which produce NO_2 (R2, R4, R7 and R8) were restricted by the presence of CO. We propose that the reason for this is the reduction of different Pd sites and NOx species in the presence of CO, since the CO reduction ability is higher than NO [56]. First we suggest a reaction where the adsorbed NO_2 on $Z^-Pd(II)Z^-$ ($Z^-Pd(II)Z^-{-}NO_2$ produced in R2) could be further reduced by CO, as shown in reaction R10. According to a previously reported DFT study, the activation barrier for $Z^-[Pd(II)OH]^+$ reduction by CO is much lower than that by NO, and importantly, the Pd species could be reduced to a lower valence [20]. Therefore, reactions R11 and R12 were added to the model to describe the consecutive reduction of $Z^-[Pd(II)OH]^+$ to $Z^-Pd(I)^+$ and Z^-H^+-Pd(0). The addition of low CO levels changes the binding strength of NO_x on Pd sites, but does not lower the NO_x adsorption capacity. It is therefore necessary to also add NO adsorption and desorption on the reduced Pd sites, i.e. NO storage on Z^-H^+-Pd(0) (reaction R13). The regeneration of Pd/SSZ-13 to its initial state after each cycle must be also considered, since the cycles are also reproducible in the presence of CO (Figures S7). Reaction R14 was therefore added to describe the reoxidation of Z^-H^+-Pd(0) to $Z^-Pd(I)^+$.

For the PdO species, three additional reactions were added into the model (reactions R15-R17). It is widely accepted that the PdOx species are easily reduced to metallic Pd as the active sites during CO oxidation [48,51,52,57]. Furthermore, given the absence of a NO_2 peak in Fig. 6A, the formation of $Pd(NO_3)_2$ was inhibited. Based on these findings, the reduction of PdO by CO (reaction R15) and the oxidation of Pd by O_2 during pretreatment (reaction R16) were added into the model. The NO adsorption on the metallic Pd site was also added (reaction R17), since the overall amount of NO_x stored did not decrease with CO addition. Note that a large amount of CO oxidation (complete conversion) was observed at high temperature. Thus a global step for CO oxidation was also added (reaction R18).

Based on the kinetic model shown in Table 3 and Table 5, the overall simulations with the existence of 200 ppm or 400 ppm CO were conducted as shown in Fig. 10. The agreement between the experimental data and model is satisfactory for both CO levels. Furthermore, mean coverages of Pd species are also provided from the simulations, as shown in Fig. 11. Compared to the coverages without CO in the inlet (Fig. 3), the fraction of all the Pd adsorption sites are changed with the existence of CO. The main change concerning $Z^-Pd(II)Z^-$ species is the ratio of absorbed NO and NO_2. After adding CO, most of the adsorbed NO_2 was reduced by CO and generated NO, leading to a higher fraction of $Z^-Pd(II)Z{-}NO$ in the adsorption branch. With the increased CO concentration, the $Z^-Pd(II)Z^-{-}NO$ fraction became higher. In the desorption branch, NO released from $Z^-Pd(II)Z^-$ at ~ 252 °C completely and left 100% empty $Z^-Pd(II)Z^-$ sites.

Regarding to the changing of $Z^-[Pd(II)OH]^+$ species with the existence of CO, Z^-H^+-Pd(0) sites were generated owing to the deeper reduction of $Z^-[Pd(II)OH]^+$ by CO. It could be seen that the $Z^-[Pd(II)OH]^+$ sites were completely reduced to $Z^-Pd(I)^-$ by CO in the NO_x adsorption branch, and the $Z^-Pd(I)^-$ sites were also partially reduced to Z^-H^+-Pd(0) (Fig. 11A). Furthermore, both of the $Z^-Pd(I)^-$ and Z^-H^+-Pd(0) sites absorbed NO in the adsorption branch. It could be seen the percentage of Z^-H^+-Pd(0) −NO reached 69% before desorption. This percentage increased to 82% when the CO concentration increased from 200 ppm to 400 ppm (Fig. 11B). When the temperature started to increase, the NO on Z^-H^+-Pd(0) −NO sites desorbed first at ~ 252 °C, then the $Z^-Pd(I)^-$ −NO sites released NO at ~ 371 °C. The empty Z^-H^+-Pd(0) sites were re-oxidized to $Z^-Pd(I)^-$ via reaction R14 at higher temperature, and $Z^-Pd(I)^-$ converted to $Z^-[Pd(II)OH]^+$ in the following pretreatment (Figure S10). Moreover, it could be inferred from these results that the presence of CO influenced more the $Z^-[Pd(II)OH]^+$ species than $Z^-Pd(II)Z^-$.

For the NOx adsorption on the PdO species in the presence of CO, there is no $Pd(NO_3)_2$ generated during NO_x adsorption and TPD, owing to that PdO sites were reduced to metallic Pd sites, which subsequently absorbed NO. When the temperature starts to increase, more PdO sites were reduced until there were no remaining PdO sites. At around 3100 s there is a sharp decrease in the fraction of Pd, which indicates the NO adsorption rate on Pd exceeds the PdO reduction rate. The Pd-NO sites released NO species at ~ 370 °C, and subsequently re-oxidized at higher temperature.

According to the coverages of Pd species under different CO concentrations (0/200/400 ppm) as shown in Fig. 3 and Fig. 11, the role of CO on passive NO_x adsorption could be clearly illustrated. With the addition of CO, the $Z^-Pd(II)Z^-{-}NO_2$ sites, which should release NO_2 at ~ 160 °C, are reduced to $Z^-Pd(II)Z^-{-}NO$. The NO on $Z^-Pd(II)Z^-$ desorbed at a higher temperature of ~ 250 °C instead. Moreover, the Pd species ($Z^-[Pd(II)OH]^+$ and PdO) were reduced by CO instead of NO. The PdO sites were reduced to metallic Pd, which shows a stronger ability to store NO than $Pd(NO_3)_2$. Thus the NO_x desorption at 166 °C, which is derived from $Pd(NO_3)_2$ decomposition, is fully inhibited. Instead, the reduced metallic Pd releases NO_x at ~ 370 °C. In addition, part of the $Z^-Pd(I)^+$ sites, which are from reduction of $Z^-[Pd(II)OH]^+$, are further reduced to Z^-H^+-Pd(0) sites. Although the interaction between NO and Z^-H^+-Pd(0) is weaker than that between NO and $Z^-Pd(I)^+$, Z^-H^+-Pd(0) still releases NO at a high temperature (~250 °C). Furthermore, the CO concentration influences the distribution of Z^-H^+-Pd(0) sites and $Z^-Pd(I)^+$ sites, resulting in a different amount of NO_x release at ~ 250 °C and 370 °C. It could be concluded that when adding CO, all the Pd species converted to the Pd sites with stronger interaction with NO_x, and therefore released

Table 5
Additional reaction steps for passive NO_x adsorption on Pd/SSZ-13 assisted with CO.

Reaction	Reaction Step	Rate formation
R10	$Z^-Pd(II)Z^-{-}NO_2 + CO \rightarrow Z^-Pd(II)Z^-{-}NO + CO_2$	$r_{10} = k_{10f}\Psi_1\theta_{S1\text{-}NO2}y_{CO}$
R11	$2Z^-[Pd(II)OH]^+ {-}NO + CO \rightarrow 2Z^-Pd(I)^+ {-}NO + H_2O + CO_2$	$r_{11} = k_{11f}(\Psi_2\theta_{S21\text{-}NO})^2 y_{CO}$
R12	$2Z^-Pd(I)^+ {-}NO + CO + H_2O \rightarrow 2Z^-H^+\text{-}Pd(0) {-}NO + CO_2$	$r_{12} = k_{12f}(\Psi_2\theta_{S22\text{-}NO})^2 y_{CO}y_{H2O}$
R13	$Z^-H^+\text{-}Pd(0) + NO \rightleftharpoons Z^-H^+\text{-}Pd(0) {-}NO$	$r_{13} = k_{13f}\Psi_2\theta_{S23}y_{NO} - k_{13b}\Psi_2\theta_{S23\text{-}NO}$
R14	$2Z^-H^+\text{-}Pd(0) + 0.5O_2 \rightleftharpoons 2Z^-Pd(I) + H_2O$	$r_{14} = k_{14f}(\Psi_2\theta_{S23})^2 y_{O2}^{0.5} - k_{14b}(\Psi_2\theta_{S22})^2 y_{H2O}$
R15	$Pd(II)O + CO \rightarrow Pd(0) + CO_2$	$r_{15} = k_{15f}\Psi_3\theta_{S31}y_{CO}$
R16	$Pd(0) + 0.5O_2 \rightarrow Pd(II)O$	$r_{16} = k_{16f}\Psi_3\theta_{S33}y_{O2}^{0.5}$
R17	$Pd(0) + NO \rightleftharpoons Pd(0) {-}NO$	$r_{17} = k_{17f}\Psi_3\theta_{S33}y_{NO} - k_{17b}\Psi_3\theta_{S33\text{-}NO}$
R18	$2CO + O_2 \rightarrow 2CO_2$	$r_{18} = k_{18f}y_{CO}^2 y_{O2}$

Storage sites:Ψ1:ZPd; Ψ2:ZPdOH; Ψ3:PdO
Storage species: S1: $Z^-Pd(II)Z^-$ S21: $Z^-[Pd(II)OH]^+$ S22: $Z^-Pd(I)$ S23: Z^-H^+-Pd(0) S31: $Pd(II)O$ S32:$Pd(NO_3)_2$ S33: Pd(0)

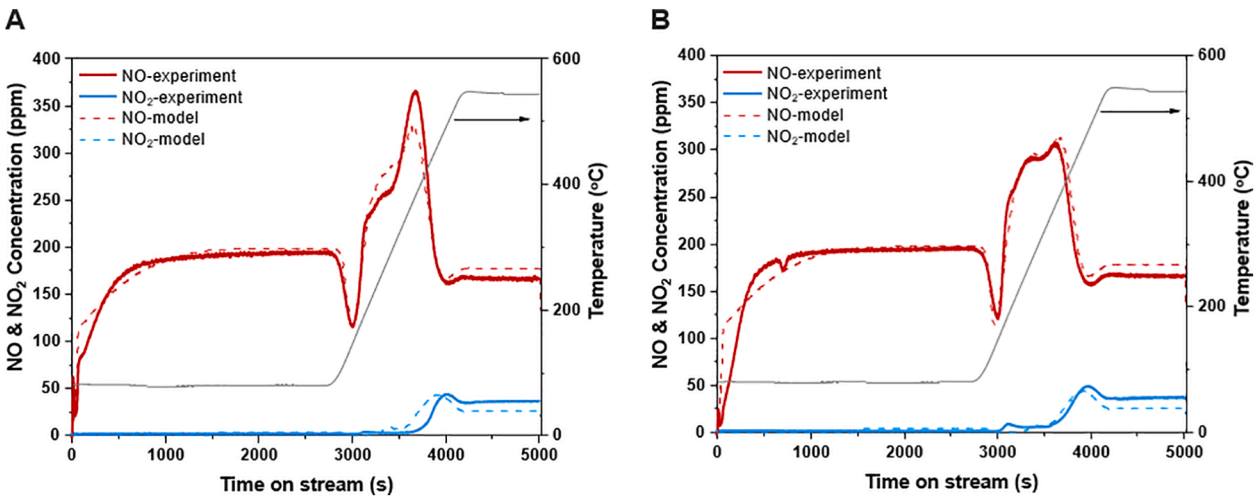

Fig. 10. Experimental and modeling results of NO_x profile using 200 ppm CO (A) and 400 ppm CO (B) in inlet.

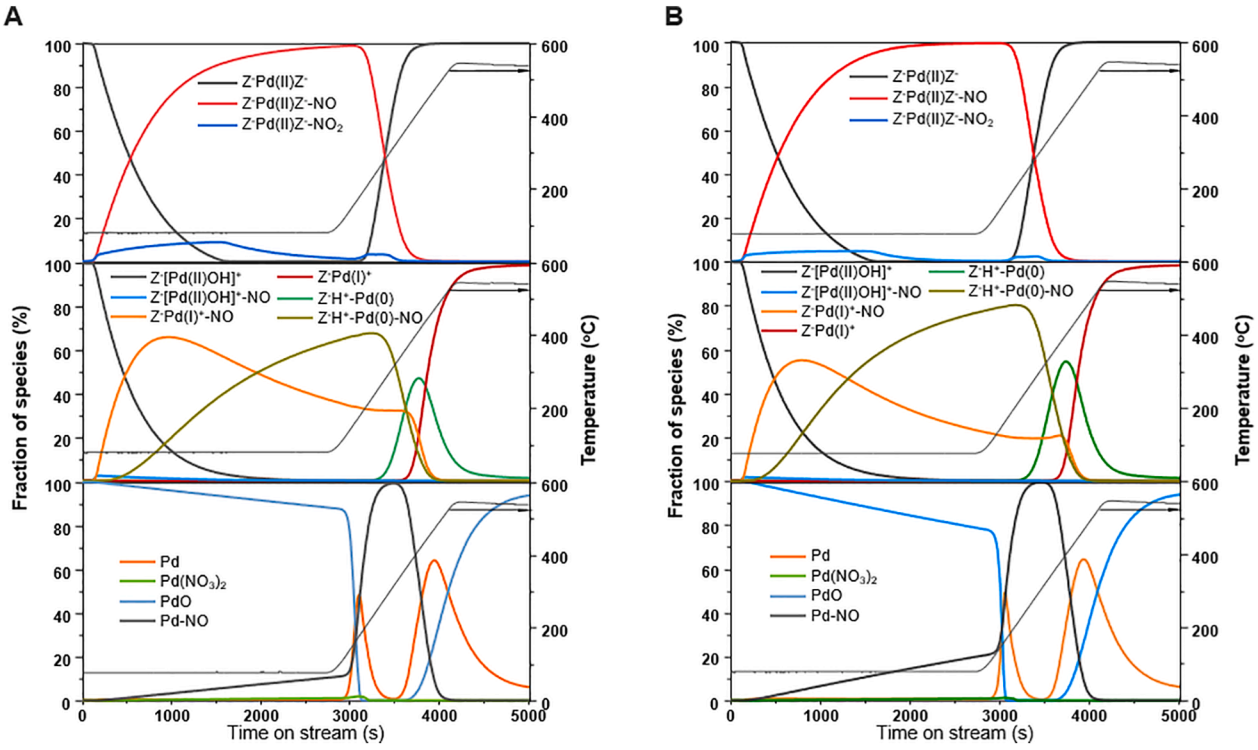

Fig. 11. Coverage (mean values) of different species on sites $Z^-Pd(II)Z^-$, $Z^-[Pd(II)OH]^+$ and PdO using 200 ppm CO (A) and 400 ppm CO (B) in inlet.

NO_x above 200 °C, which is favorable for urea dosing [7,8] for the downstream SCR treatment.

The model was further verified by PNA multi-cycle tests with different inlet CO concentration (the procedure is shown in Table S1, test 2, Cycle 1–4). Figure S11A shows the inlet NO_x concentration and reaction temperature, and Figure S11B shows the corresponding outlet NO & NO_2 concentration in the model and experiment. Moreover, the magnified results of cycle 2 and cycle 4 were shown in Figure S11C-D. The developed model could well describe the multi-cycle PNA test using different inlet feed gas (Fig. 4 and Figure S11).

4.6. Full-scale converter modeling of PNA

The reaction mechanism discussed in the previous sections is based on a small catalyst sample, in which any kind of spatial non-uniformities is avoided. This is very important for developing the reaction kinetics. When applying a PNA coating to a real-life sized catalyst, the intrinsic reaction mechanism is overlaid with non-idealities such as radially non-uniform inlet flow distributions and non-uniform converter temperatures. Assuming a reasonably high inlet flow uniformity, 1D catalyst models are well suited to assess the behavior of the PNA reaction mechanism on converter level during a transient cold-start phase.

Here we consider an 8.5 L cordierite converter with a length of 152 mm and a diameter of 266 mm, a channel density of 400 CPSI and a wall thickness of 6 mil. The converter is initialized with a temperature of –7°C and it is assumed that the converter is purged. The catalyst is fed with a mass flow of 300 kg/h (i.e. space velocity of around 50000 h^{-1}) and a constant gas composition of 200 ppm NO, 5 ppm NO_2, 400 ppm CO, 8% O_2 and 5% H_2O in nitrogen. The inlet temperature follows a pattern of four different phases. Between 0 s and 10 s, the temperature is

constant at –7°C, between 10 s and 50 s it ramps up to 220 °C and it is held constant for another 50 s. The fourth phase is initiated with an instantaneous temperature step from 220 °C to 450 °C that is held constant until the end of the simulation. Fig. 12 summarizes the four selected responses of the catalyst during this transient heat-up scenario.

Fig. 12a shows the catalyst substrate temperature over its relative length and versus the simulation time. In the time direction, the temperature profile follows the applied inlet boundary conditions reflecting the different heat-up phases. It can be observed that the substrate temperature near the catalyst inlet (i.e. relative position is zero) follows the inlet gas temperature during the ramp-up phases with steeper gradients than at the outlet of the catalyst. Near the outlet, the substrate temperature also features a slightly delayed heat-up. This behavior can be explained by the thermal inertia of the converter, where the heat-up gradients are mainly a result of the substrate material and the inlet temperature and mass flow conditions. Further, the temperature profile shows no specific regions that can be associated with pronounced heat of reactions. This is in line with the modeling assumption during the kinetic model development, that the reaction heat of the applied reactions is negligible.

Fig. 12b shows the change of NO_x concentration in the gas phase over converter length and time. During the first approximately 25 s, no dedicated NOx storage takes place as the outlet concentration features the values of the inlet concentration. In the time period between 25 s and 75 s, the NO_x outlet concentration goes down to zero and back up to the inlet value. This indicates that the NO_x storage reactions become active at around 100 °C (compare Fig. 12a). NOx becomes stored and the storages sites are completely filled after a storage phase of about 50 s. These results are in line with the experimental studies by Chen et al [11], where Pd/CHA exhibited a low rate for NO_x storage at low temperature. The time for 90% efficiency at about 80 °C was 0 for Pd/CHA, but there was still a substantial overall storage at this temperature [11]. This is also seen in our experiment (see Fig. 12), where NO_x breaks through immediately during the adsorption phase, which is followed by a slower NO_x uptake.

The storage duration can be interpreted as a result of the applied catalyst size, the amount of active storage sites and the NO_x feed flow. When the catalyst enters the second heat-up phase (time = 100 s) a distinct increase of the NO_x outlet concentrations can be observed. As soon as the substrate temperatures reach values around 350 °C, NOx desorbs from the surface into the gas bulk and is transported out of the catalyst. The desorption ends when all storage sites are emptied. Further, the NO_x concentration returns from the peak values to the inlet value in a much faster time near the catalyst inlet than near the outlet. This can be explained by spatial temperature non-uniformities. How spatial temperature non-uniformities influence the storage behavior of NO and NO_x is depicted in Fig. 12c and Fig. 12d, respectively. It can be observed that the significant storage of NO and NO_x starts at temperatures of around 100 °C and that the storage takes place first near the catalyst inlet followed by storage sites located further downstream. This can be explained by temperature maldistributions and by a dilution effect. Storage sites further downstream the catalyst are exposed to NOx from the gas bulk only when storage sites in the upstream direction are filled up. When entering the second heat-up phase (time = 100 s) the stored NO fraction slightly increases, driven by the temperature and then decreases with a sharp gradient, coinciding with the peak of the NO_x concentration in the gas bulk (compare Fig. 12b). The amount of stored NO_x shows a similar pattern as the stored NO, whereas during the phase of constant inlet temperature (50 s < time < 100 s) more pronounced spatial maldistributions can be seen. The stored NO_x features a ~ 25% higher level in the first 30% of the catalyst than in the second two-thirds of the converter. The reason for this can be found in the storage behavior of NO_2, which is the main contributor to the storage occurring on the $Z^-Pd(II)Z^-$ site. NO_2 is absorbed from the initial temperature and starts already to desorb again at around 170 °C. This, in combination with the lower NO_2 input level leads to more pronounced uniformities when comparing the NO_x storage to NO storage.

A further insight in the spatial and temporal resolved behavior of three different storage sites is presented in Figure S12. It could be seen that the change of the Pd species is slightly different from those in the small model catalyst (Fig. 11), which mainly results from the different temperature distributions. Owing to the low NO adsorption rate on $Z^-Pd(II)Z^-$ and $Z^-[Pd(II)OH]^+$, these two sites were not saturated in the first 200 s, where the temperature reached 220 °C and was kept constant for 50 s. Instead, with the increased temperature, most of $Z^-[Pd(II)OH]^+$ species were reduced by CO to generate $Z^-Pd(I)^+$, which shows a higher NO adsorption rate. Therefore, the NO_x adsorption rate increased with the temperature ramping (10–50 s), in accordance with NO_x profile as shown in Fig. 12. Furthermore, the Z^-H^+-Pd(0) species were seldom produced by $Z^-Pd(I)^+$ reduction owing to the short time for reaction. For

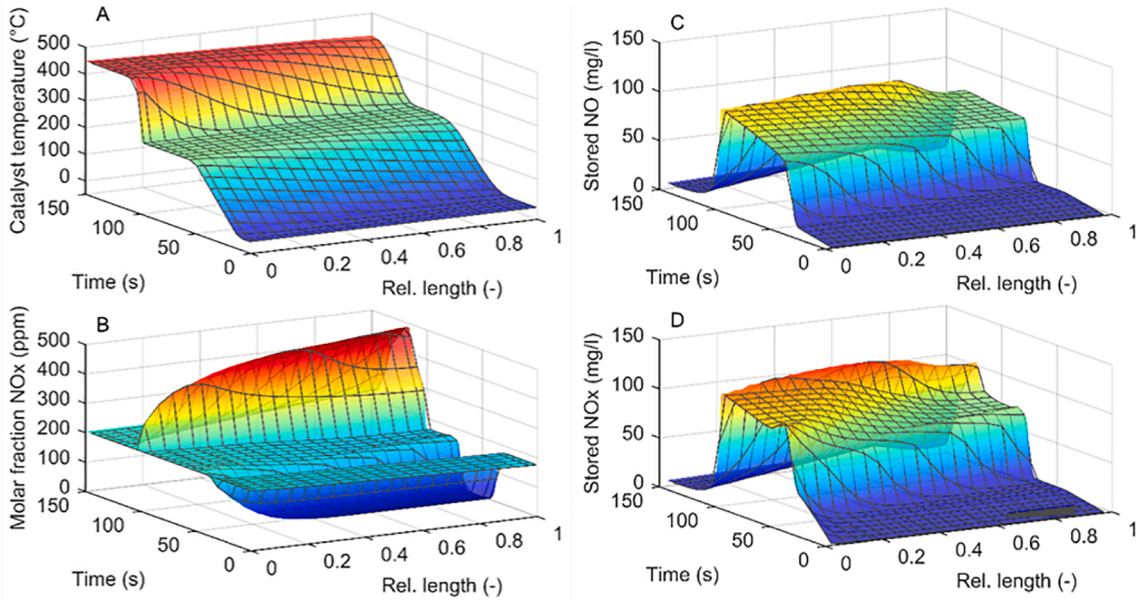

Fig. 12. Spatial and temporal resolved PNA converter behavior during a transient cold-start. A: substrate temperature, B: NO_x concentration in the gas bulk and C, D: stored amount of NO and NO_x.

the PdO species, $Pd(NO_3)_2$ was also seldom produced because most of PdO species were reduced to metallic Pd instead. This also contributed to the increased NO adsorption rate when the temperature started to increase (10–50 s). It could be found that the stored species profile downstream is slightly delayed compared to the inlet, resulting from the temperature maldistributions and the dilution effect.

5. Conclusions

In this work, a kinetic model was developed to describe CO assisted passive NO_x adsorption. Pd/SSZ-13 was first synthesized as a PNA and then tested for multi-cycle NO_x adsorption and TPD, under different gas conditions (200–400 ppm NO, 0–400 ppm CO, 5%H_2O, 8%O_2 balanced in Ar). Combining the NO_x adsorption and TPD test as well as characterizations of Pd species on Pd/SSZ-13, it was found that the presence of CO increased the NO_x desorption temperature, while the NO_x adsorption amount was similar. It was also found that the amount of CO adsorbed on Pd/SSZ-13 was very low, compared to the NO_x desorption. These results indicate that there was no or only minor (CO)(NO) bi-absorbed species on the Pd surface. XPS revealed that Pd species were reduced by CO to lower chemical states and we propose that this is the reason for the increased stability of the stored NO_x in our experiments. Based on the experimental results, a kinetic model with three initial Pd sites ($Z^-Pd(II)Z^-$, $Z^-[Pd(II)OH]^+$ and PdO) was developed for the cycling experiments when changing the NO_x concentrations, without the presence of CO. In the presence of CO, the addition of reactions for reducing the palladium species, to $Z^-Pd(I)^+$ and Z^-H^+-Pd(0) and metallic Pd, were critical. The model successfully described the multi-cycle NO_x adsorption and TPD processes under different gas conditions (200–400 ppm NO, 0–400 ppm CO, 5%H_2O, 8%O_2 balanced in Ar), which simulates multiple cold start periods.

The kinetic model also described the change of Pd species during NO_x adsorption and TPD. For the NO_x adsorption and TPD without CO, $Z^-Pd(II)Z^-$, $Z^-[Pd(II)OH]^+$ and PdO mainly absorbed NO to form $Z^-Pd(II)Z^-{-}NO$, $Z^-[Pd(II)OH]^+$ $-NO$ and $Pd(NO_3)_2$. Furthermore, the small amount of NO_2 in the feed gas also absorbed on $Z^-Pd(II)Z^-$. During the TPD period, $Z^-Pd(II)Z^-{-}NO$ and $Z^-Pd(I)^+$ $-NO$, which is produced from the reduction of $Z^-[Pd(II)OH]^+$ $-NO$, released NO_x above 200 °C, while $Pd(NO_3)_2$ and $Z^-Pd(II)Z^-{-}NO_2$ released NO_x below 200 °C. With the addition of 200 ~ 400 ppm CO, $Z^-[Pd(II)OH]^+$ and PdO were respectively reduced by CO to generate $Z^-Pd(I)^+$, Z^-H^+-Pd(0) and metallic Pd, all of which could absorb NO species and release them above 200 °C. The $Z^-Pd(II)Z{-}NO_2$ is also reduced by CO to form $Z^-Pd(II)Z^-{-}NO$ and releases NO above 200 °C. Using a combination of experiments and kinetic modelling, a detailed mechanism for the roles of CO in passive NO_x adsorption has been derived. This model was thereafter used to simulate a real-size catalytic converter, illustrating the effects of temperature and NO_x profiles during cold-start simulations. The system level simulation results revealed two essential findings. The implementation of the proposed reaction scheme works for different operating conditions in a robust manner and the thermal converter model is key to correctly assess the PNA performance under real-life conditions.

Declaration of Competing Interest

The authors declare that they have no known competing financial interests or personal relationships that could have appeared to influence the work reported in this paper.

Acknowledgments

This study was performed at the Competence Center for Catalysis, Chemical Engineering at Chalmers University in collaboration with AVL. This project has received funding from the European Union's Horizon 2020 research and innovation programme under grant agreement no 874972. We thank Dr. Thomas Mitterfellner and Anton Nahtigal from AVL List GmbH for the help with AVL BOOST, Dr. Eric Tam and Dr. Ludvig de Knoop from Chalmers material characterization laboratory, Chalmers University of Technology for their help with XPS and ESEM.

Appendix A. Supplementary data

Supplementary data to this article can be found online at https://doi.org/10.1016/j.cej.2021.132459.

References

[1] A. Wang, L. Olsson, The impact of automotive catalysis on the United Nations sustainable development goals, Nature Catal. 2 (7) (2019) 566–570, https://doi.org/10.1038/s41929-019-0318-3.
[2] A. Marberger, A.W. Petrov, P. Steiger, M. Elsener, O. Kröcher, M. Nachtegaal, D. Ferri, Time-resolved copper speciation during selective catalytic reduction of NO on Cu-SSZ-13, Nature Catal. 1 (3) (2018) 221–227, https://doi.org/10.1038/s41929-018-0032-6.
[3] C. Paolucci, I. Khurana, A.A. Parekh, S.C. Li, A.J. Shih, H. Li, J.R. Di Iorio, J. D. Albarracin-Caballero, A. Yezerets, J.T. Miller, W.N. Delgass, F.H. Ribeiro, W. F. Schneider, R. Gounder, Dynamic multinuclear sites formed by mobilized copper ions in NOx selective catalytic reduction, Science 357 (6354) (2017) 898–903, https://doi.org/10.1126/science.aan5630.
[4] C.H. Kim, G.S. Qi, K. Dahlberg, W. Li, Strontium-doped perovskites rival platinum catalysts for treating nox in simulated diesel exhaust, Science 327 (5973) (2010) 1624–1627, https://doi.org/10.1126/science.1184087.
[5] B.S. Kim, H. Jeong, J. Bae, P.S. Kim, C.H. Kim, H. Lee, Lean NOx trap catalysts with high low-temperature activity and hydrothermal stability, Appl. Catal. B-Environ. 270 (2020) 9, https://doi.org/10.1016/j.apcatb.2020.118871.
[6] J. Lee, J.R. Theis, E.A. Kyriakidou, Vehicle emissions trapping materials: Successes, challenges, and the path forward, Appl. Catal. B-Environ. 243 (2019) 397–414, https://doi.org/10.1016/j.apcatb.2018.10.069.
[7] K. Khivantsev, N.R. Jaegers, L. Kovarik, J.C. Hanson, F.(. Tao, Y.u. Tang, X. Zhang, I.Z. Koleva, H.A. Aleksandrov, G.N. Vayssilov, Y. Wang, F. Gao, J. Szanyi, Achieving atomic dispersion of highly loaded transition metals in small-pore zeolite SSZ-13: High-capacity and high-efficiency low-temperature CO and passive NOx adsorbers, Angew. Chem. Int. Ed. 57 (51) (2018) 16672–16677, https://doi.org/10.1002/anie.v57.5110.1002/anie.201809343.
[8] Y. Ryou, J. Lee, S.J. Cho, H. Lee, C.H. Kim, D.H. Kim, Activation of Pd/SSZ-13 catalyst by hydrothermal aging treatment in passive NO adsorption performance at low temperature for cold start application, Appl. Catal. B-Environ. 212 (2017) 140–149, https://doi.org/10.1016/j.apcatb.2017.04.077.
[9] Y. Gu, W.S. Epling, Passive NOx adsorber: An overview of catalyst performance and reaction chemistry, Appl. Catal. A-Gen. 570 (2019) 1–14, https://doi.org/10.1016/j.apcata.2018.10.036.
[10] A. Wang, K. Xie, A. Kumar, K. Kamasamudram, L. Olsson, Layered Pd/SSZ-13 with Cu/SSZ-13 as PNA – SCR dual-layer monolith catalyst for NOx abatement, Catal. Today 360 (2021) 356–366, https://doi.org/10.1016/j.cattod.2020.01.035.
[11] H.Y. Chen, J.E. Collier, D. Liu, L. Mantarosie, D. Durán-Martín, V. Novák, R. R. Rajaram, D. Thompsett, Low temperature NO storage of zeolite supported Pd for low temperature diesel engine emission control, Catalysis Letters 146 (9) (2016) 1706–1711, https://doi.org/10.1007/s10562-016-1794-6.
[12] Y. Zheng, L. Kovarik, M.H. Engelhard, Y. Wang, Y. Wang, F. Gao, J. Szanyi, Low-temperature Pd/zeolite passive NOx adsorbers: structure, performance, and adsorption chemistry, J Phys. Chem. C 121 (29) (2017) 15793–15803, https://doi.org/10.1021/acs.jpcc.7b0431210.1021/acs.jpcc.7b04312.s001.
[13] K. Khivantsev, F. Gao, L. Kovarik, Y. Wang, J. Szanyi, Molecular level understanding of how oxygen and carbon monoxide improve NOx storage in palladium/SSZ-13 passive NOx adsorbers: The role of NO^+ and Pd(II)(CO)(NO) Species, J Phys. Chem. C 122 (20) (2018) 10820–10827, https://doi.org/10.1021/acs.jpcc.8b0100710.1021/acs.jpcc.8b01007.s001.
[14] R.F. Ilmasani, J. Woo, D. Creaser, L. Olsson, Influencing the NOx stability by metal oxide addition to Pd/BEA for passive NOx adsorbers, Ind. Eng. Chem. Res. 59 (21) (2020) 9830–9840, https://doi.org/10.1021/acs.iecr.9b06976.
[15] A. Wang, K. Lindgren, M. Di, D. Bernin, P.-A. Carlsson, M. Thuvander, L. Olsson, Insight into hydrothermal aging effect on Pd sites over Pd/LTA and Pd/SSZ-13 as PNA and CO oxidation monolith catalysts, Appl. Catal. B-Environ. 278 (2020) 119315, https://doi.org/10.1016/j.apcatb.2020.119315.
[16] M. Ambast, K. Karinshak, B.M.M. Rahman, L.C. Grabow, M.P. Harold, Passive NOx adsorption on Pd/H-ZSM-5: Experiments and modeling, Appl. Catal. B-Environ. 269 (2020) 118802, https://doi.org/10.1016/j.apcatb.2020.118802.
[17] K. Mandal, Y. Gu, K.S. Westendorff, S. Li, J.A. Pihl, L.C. Grabow, W.S. Epling, C. Paolucci, Condition-dependent Pd speciation and NO adsorption in Pd/zeolites, ACS Catal. 10 (21) (2020) 12801–12818, https://doi.org/10.1021/acscatal.0c0358510.1021/acscatal.0c03585.s00110.1021/acscatal.0c03585.s002.
[18] K. Chakarova, E. Ivanova, K. Hadjiivanov, D. Klissurski, H. Knözinger, Coordination chemistry of palladium cations in Pd-H-ZSM-5 as revealed by FTIR spectra of adsorbed and co-adsorbed probe molecules (CO and NO), Phys. Chem. Chem. Phys. 006 (13) (2004) 3702–3709, https://doi.org/10.1039/b401934b.
[19] A. Vu, J. Luo, J. Li, W.S. Epling, Effects of CO on Pd/BEA Passive NOx Adsorbers, Catalysis Letters 147 (3) (2017) 745–750, https://doi.org/10.1007/s10562-017-1976-x.

[20] D. Mei, F. Gao, J. Szanyi, Y. Wang, Mechanistic insight into the passive NOx adsorption in the highly dispersed Pd/HBEA zeolite, Appl. Catal. A-Gen. 569 (2019) 181–189, https://doi.org/10.1016/j.apcata.2018.10.037.

[21] A. Gupta, S.B. Kang, M.P. Harold, NOx uptake and release on Pd/SSZ-13: Impact Of Feed composition and temperature, Catal. Today 360 (2021) 411–425, https://doi.org/10.1016/j.cattod.2020.01.018.

[22] Y. Gu, R.P. Zelinsky, Y.-R. Chen, W.S. Epling, Investigation of an irreversible NOx storage degradation Mode on a Pd/BEA passive NOx adsorber, Appl. Catal. B-Environ. 258 (2019) 118032, https://doi.org/10.1016/j.apcatb.2019.118032.

[23] M. Ambast, A. Gupta, B.M.M. Rahman, L.C. Grabow, M.P. Harold, NOx adsorption with CO and C_2H_4 on Pd/SSZ-13: Experiments and modeling, Appl. Catal. B-Environ. 286 (2021) 119871, https://doi.org/10.1016/j.apcatb.2020.119871.

[24] A. Kvasničková, P. Kočí, Y. Ji, M. Crocker, Effective model of NOx adsorption and desorption on PtPd/CeO_2-ZrO_2 passive NOx Adsorber, Catal. Letters 150 (11) (2020) 3223–3233, https://doi.org/10.1007/s10562-020-03186-z.

[25] U. Deka, A. Juhin, E.A. Eilertsen, H. Emerich, M.A. Green, S.T. Korhonen, B. M. Weckhuysen, A.M. Beale, Confirmation of isolated Cu^{2+} ions in SSZ-13 zeolite as active sites in NH_3-selective catalytic reduction, J Phys. Chem. C 116 (7) (2012) 4809–4818, https://doi.org/10.1021/jp212450d.

[26] F. Gao, N.M. Washton, Y. Wang, M. Kollár, J. Szanyi, C.H.F. Peden, Effects of Si/Al ratio on Cu/SSZ-13 NH3-SCR catalysts: Implications for the active Cu species and the roles of Brønsted acidity, J Catal. 331 (2015) 25–38, https://doi.org/10.1016/j.jcat.2015.08.004.

[27] K. Wijayanti, S. Andonova, A. Kumar, J. Li, K. Kamasamudram, N.W. Currier, A. Yezerets, L. Olsson, Impact of sulfur oxide on NH_3-SCR over Cu-SAPO-34, Appl. Catal. B-Environ. 166–167 (2015) 568–579, https://doi.org/10.1016/j.apcatb.2014.11.043.

[28] S. Chen, M.A. Vasiliades, Q. Yan, G. Yang, X. Du, C. Zhang, Y. Li, T. Zhu, Q. Wang, A.M. Efstathiou, Remarkable N_2-selectivity enhancement of practical NH_3-SCR over $Co_{0.5}Mn_1Fe_{0.25}Al_{0.75}O_x$-LDO: The role of Co investigated by transient kinetic and DFT mechanistic studies, Appl. Catal. B: Environ. 277 (2020) 119186, https://doi.org/10.1016/j.apcatb.2020.119186.

[29] Q. Yan, Y. Gao, Y. Li, M.A. Vasiliades, S. Chen, C. Zhang, R. Gui, Q. Wang, T. Zhu, A.M. Efstathiou, Promotional effect of Ce doping in $Cu_4Al_1O_x$ – LDO catalyst for low-T practical NH_3-SCR: Steady-state and transient kinetics studies, Appl. Catal. B: Environ. 255 (2019) 117749, https://doi.org/10.1016/j.apcatb.2019.117749.

[30] F. Gramigni, N.D. Nasello, N. Usberti, U. Iacobone, T. Selleri, W. Hu, S. Liu, X. Gao, I. Nova, E. Tronconi, Transient kinetic analysis of low-temperature NH_3-SCR over Cu-CHA catalysts reveals a quadratic dependence of Cu reduction rates on CuII, ACS Catal. 11 (8) (2021) 4821–4831, https://doi.org/10.1021/acscatal.0c0536210.1021/acscatal.0c05362.s001.

[31] A.L. GmbH, AVL BOOST Aftertreatment Manual (2020).

[32] D. Chatterjee, T. Burkhardt, B. Bandl-Konrad, T. Braun, E. Tronconi, I. Nova, C. Ciardelli, Numerical simulation of ammonia SCR-catalytic converters: Model development and application, SAE Transactions 114 (2005) 437–448.

[33] S. Tamm, L. Olsson, S. Fogel, P. Gabrielsson, M. Skoglundh, A kinetic model of the hydrogen assisted selective catalytic reduction of NO with ammonia over Ag/Al_2O_3, AIChE J. 59 (11) (2013) 4325–4333, https://doi.org/10.1002/aic.14170.

[34] L. Olsson, K. Wijayanti, K. Leistner, A. Kumar, S.Y. Joshi, K. Kamasamudram, N. W. Currier, A. Yezerets, A multi-site kinetic model for NH3-SCR over Cu/SSZ-13, Appl. Catal. B-Environ. 174–175 (2015) 212–224, https://doi.org/10.1016/j.apcatb.2015.02.037.

[35] L. Olsson, H. Sjövall, R.J. Blint, A kinetic model for ammonia selective catalytic reduction over Cu-ZSM-5, Appl. Catal. B-Environ. 81 (3–4) (2008) 203–217, https://doi.org/10.1016/j.apcatb.2007.12.011.

[36] Supriyanto, K. Wijayanti, A. Kumar, S. Joshi, K. Kamasamudram, N.W. Currier, A. Yezerets, L. Olsson, Olsson, Global kinetic modeling of hydrothermal aging of NH3-SCR over Cu-zeolites, Appl. Catal. B-Environ. 163 (2015) 382–392, https://doi.org/10.1016/j.apcatb.2014.07.059.

[37] L. Olsson, K. Wijayanti, K. Leistner, A. Kumar, S.Y. Joshi, K. Kamasamudram, N. W. Currier, A. Yezerets, A kinetic model for sulfur poisoning and regeneration of Cu/SSZ-13 used for NH_3-SCR, Appl. Catal. B-Environ. 183 (2016) 394–406, https://doi.org/10.1016/j.apcatb.2015.11.001.

[38] A. Wang, P. Arora, D. Bernin, A. Kumar, K. Kamasamudram, L. Olsson, Investigation of the robust hydrothermal stability of Cu/LTA for NH3-SCR reaction, Appl. Catal. B-Environ. 246 (2019) 242–253, https://doi.org/10.1016/j.apcatb.2019.01.039.

[39] L. Olsson, M. Fredriksson, R.J. Blint, Kinetic modeling of sulfur poisoning and regeneration of lean NOx traps, Appl. Catal. B-Environ. 100 (1–2) (2010) 31–41, https://doi.org/10.1016/j.apcatb.2010.07.004.

[40] X. Auvray, W. Partridge, J.-S. Choi, J. Pihl, F. Coehlo, A. Yezerets, K. Kamasamudram, N. Currier, L. Olsson, Kinetic modeling of NH_3-SCR over a supported Cu zeolite catalyst using axial species distribution measurements, Appl. Catal. B-Environ. 163 (2015) 393–403, https://doi.org/10.1016/j.apcatb.2014.08.003.

[41] R. Kee, G. Dixon-lewis, J. Warnatz, M. Coltrin, J. Miller, A fortran computer code package for the evaluation of gas-phase multicomponent transport properties, Sandia Report SAND86-8246 (1986).

[42] L. Olsson, H. Sjövall, R.J. Blint, Detailed kinetic modeling of NOx adsorption and NO oxidation over Cu-ZSM-5, Appl. Catal. B-Environ. 87 (3) (2009) 200–210, https://doi.org/10.1016/j.apcatb.2008.09.007.

[43] J. Xu, M.P. Harold, V. Balakotaiah, Modeling the effects of Pt loading on NOx storage on Pt/BaO/Al2O3 catalysts, Appl. Catal. B-Environ. 104 (3–4) (2011) 305–315, https://doi.org/10.1016/j.apcatb.2011.03.014.

[44] Y. Ryou, J. Lee, Y. Kim, S. Hwang, H. Lee, C.H. Kim, D.H. Kim, Effect of reduction treatments (H_2 vs. CO) on the NO adsorption ability and the physicochemical properties of Pd/SSZ-13 passive NOx adsorber for cold start application, Appl. Catal. A-Gen. 569 (2019) 28–34, https://doi.org/10.1016/j.apcata.2018.10.016.

[45] Y. Ji, S. Bai, M. Crocker, Al_2O_3-based passive NOx adsorbers for low temperature applications, Appl. Catal. B-Environ. 170–171 (2015) 283–292, https://doi.org/10.1016/j.apcatb.2015.01.025.

[46] J. Lee, Y. Ryou, S.J. Cho, H. Lee, C.H. Kim, D.H. Kim, Investigation of the active sites and optimum Pd/Al of Pd/ZSM–5 passive NO adsorbers for the cold-start application: Evidence of isolated-Pd species obtained after a high-temperature thermal treatment, Appl. Catal. B-Environ. 226 (2018) 71–82, https://doi.org/10.1016/j.apcatb.2017.12.031.

[47] W.-C. Ding, X.-K. Gu, H.-Y. Su, W.-X. Li, Single Pd atom embedded in CeO_2(111) for NO reduction with CO: A first-principles study, J. Phys. Chem. C 118 (23) (2014) 12216–12223, https://doi.org/10.1021/jp503745c.

[48] E. Sasmaz, C. Wang, M.J. Lance, J. Lauterbach, In situ spectroscopic investigation of a Pd local structure over Pd/CeO2 and Pd/MnOx–CeO2 during CO oxidation, J. Mater. Chem. A 5 (25) (2017) 12998–13008, https://doi.org/10.1039/C7TA00696A.

[49] S.M. Lang, T. Schnabel, T.M. Bernhardt, Reactions of carbon monoxide with free palladium oxide clusters: strongly size dependent competition between adsorption and combustion, Phys. Chem. Chem. Phys. 14 (26) (2012) 70–9364, https://doi.org/10.1039/c2cp23976k.

[50] S. Yasumura, H. Ide, T. Ueda, Y. Jing, C. Liu, K. Kon, T. Toyao, Z. Maeno, K.-I. Shimizu, Transformation of bulk Pd to Pd cations in small-pore CHA zeolites facilitated by NO, JACS Au 1 (2) (2021) 201–211, https://doi.org/10.1021/jacsau.0c0011210.1021/jacsau.0c00112.s00110.1021/jacsau.0c00112.s002.

[51] Y. Li, Y. Yu, J.-G. Wang, J. Song, Q. Li, M. Dong, C.-J. Liu, CO oxidation over graphene supported palladium catalyst, Appl. Catal. B-Environ. 125 (2012) 189–196, https://doi.org/10.1016/j.apcatb.2012.05.023.

[52] A.S. Ivanova, E.M. Slavinskaya, R.V. Gulyaev, V.I. Zaikovskii, O.A. Stonkus, I. G. Danilova, L.M. Plyasova, I.A. Polukhina, A.I. Boronin, Metal–support interactions in Pt/Al_2O_3 and Pd/Al_2O_3 catalysts for CO oxidation, Appl. Catal. B-Environ. 97 (1–2) (2010) 57–71, https://doi.org/10.1016/j.apcatb.2010.03.024.

[53] L.S. Kibis, A.I. Stadnichenko, S.V. Koscheev, V.I. Zaikovskii, A.I. Boronin, Highly oxidized palladium nanoparticles comprising Pd^{4+} species: Spectroscopic and structural aspects, thermal stability, and reactivity, J Phys. Chem. C 116 (36) (2012) 19342–19348, https://doi.org/10.1021/jp305166k.

[54] X. Liu, D. Tian, S. Ren, C. Meng, Structure sensitivity of NO adsorption–dissociation on Pd_n (n = 8, 13, 19, 25) clusters, J Phys. Chem. C 119 (23) (2015) 12941–12948, https://doi.org/10.1021/acs.jpcc.5b01141.

[55] K. Honkala, P. Pirilä, K. Laasonen, CO and NO adsorption and co-adsorption on the Pd(111) surface, Surf. Sci. 489 (1-3) (2001) 72–82.

[56] F. Ahmed, R. Nagumo, R. Miura, A. Suzuki, H. Tsuboi, N. Hatakeyama, H. Takaba, A. Miyamoto, CO oxidation and NO reduction on a MgO(100) supported Pd cluster: A quantum chemical molecular dynamics study, J Phys. Chem. C 115 (49) (2011) 24123–24132, https://doi.org/10.1021/jp204348e.

[57] A. Marikutsa, M. Rumyantseva, A. Gaskov, Specific interaction of PdOx- and RuOy-modified tin dioxide with CO and NH_3 gases: kelvin probe and DRIFT studies, J Phys. Chem. C 119 (43) (2015) 24342–24350, https://doi.org/10.1021/acs.jpcc.5b02532.